

# Two distinct halo populations in the solar neighborhood

## III. Evidence from stellar ages and orbital parameters <sup>\*,\*\*</sup>

W. J. Schuster<sup>1</sup>, E. Moreno<sup>2</sup>, P. E. Nissen<sup>3</sup>, and B. Pichardo<sup>2</sup>

<sup>1</sup> Observatorio Astronómico Nacional, Universidad Nacional Autónoma de México, Apartado Postal 877, C.P. 22800 Ensenada, B.C., México. e-mail: [schuster@astrocen.unam.mx](mailto:schuster@astrocen.unam.mx)

<sup>2</sup> Instituto de Astronomía, Universidad Nacional Autónoma de México, A.P. 70-264, 04510, México, D.F., México. e-mail: [edmundo@astroscu.unam.mx](mailto:edmundo@astroscu.unam.mx); [barbara@astroscu.unam.mx](mailto:barbara@astroscu.unam.mx)

<sup>3</sup> Department of Physics and Astronomy, University of Aarhus, DK-8000 Aarhus C, Denmark. e-mail: [pen@phys.au.dk](mailto:pen@phys.au.dk)

Received / Accepted

### ABSTRACT

**Context.** In Papers I and II of this series, we have found clear indications of the existence of two distinct populations of stars in the solar neighborhood belonging to the metal-rich end of the halo metallicity distribution function. Based on high-resolution, high S/N spectra, it is possible to distinguish between 'high-alpha' and 'low-alpha' components using the  $[\alpha/\text{Fe}]$  versus  $[\text{Fe}/\text{H}]$  diagram.

**Aims.** Precise relative ages and orbital parameters are determined for 67 halo and 16 thick-disk stars having metallicities in the range  $-1.4 < [\text{Fe}/\text{H}] < -0.4$  to better understand the context of the two halo populations in the formation and evolution of the Galaxy.

**Methods.** Ages are derived by comparing the positions of stars in the  $\log T_{\text{eff}} - \log g$  diagram with isochrones from the  $Y^2$  models interpolated to the exact  $[\text{Fe}/\text{H}]$  and  $[\alpha/\text{Fe}]$  values of each star. The stellar parameters have been adopted from the preceding spectroscopic analyses, but possible systematic errors in  $T_{\text{eff}}$  and  $\log g$  are considered and corrected. With space velocities from Paper I as initial conditions, orbital integrations have been carried out using a detailed, observationally constrained Milky Way model including a bar and spiral arms.

**Results.** The 'high-alpha' halo stars have ages 2–3 Gyr larger than the 'low-alpha' ones, with some probability that the thick-disk stars have ages intermediate between these two halo components. The orbital parameters show very distinct differences between the 'high-alpha' and 'low-alpha' halo stars. The 'low-alpha' ones have  $r_{\text{max}}$ 's to 30–40 kpc,  $z_{\text{max}}$ 's to  $\approx 18$  kpc, and  $e_{\text{max}}$ 's clumped at values greater than 0.85, while the 'high-alpha' ones,  $r_{\text{max}}$ 's to about 16 kpc,  $z_{\text{max}}$ 's to 6–8 kpc, and  $e_{\text{max}}$  values more or less uniformly distributed over 0.4–1.0.

**Conclusions.** A dual *in situ*-plus-accretion formation scenario best explains the existence and characteristics of these two metal-rich halo populations, but one remaining defect is that this model is not consistent regarding the  $r_{\text{max}}$ 's obtained for the *in situ* 'high-alpha' component; the predicted values are too small. It appears that  $\omega$  Cen may have contributed in a significant way to the existence of the 'low-alpha' component; recent models, including dynamical friction and tidal stripping, have produced results consistent with the present mass and orbital characteristics of  $\omega$  Cen, while at the same time including extremes in the orbital parameters as great as those of the 'low-alpha' component.

**Key words.** Stars: abundances – Stars: kinematics – Galaxy: halo – Galaxy: formation

## 1. Introduction

A stellar population is characterized by the distribution in space, kinematics, age, and chemical composition of its members. Probably, the stars in a population have a common origin and history. Unraveling the various Galactic populations is therefore of high importance for understanding the formation and evolution of the Galaxy. In this context, it has been much discussed if the Galactic halo consists

of more than one population. In the classic confrontation of early Galactic models, the monolithic collapse model of Eggen, Lynden-Bell & Sandage (1962, ELS) corresponded to a single halo population, while from a study of globular cluster horizontal branches, Searle and Zinn (1978, SZ) suggested that the outer globular clusters have a wider range in ages than the inner ones, and that they represent accretion events which continued for some time after the inner collapse. Later, Zinn (1993) proposed that the Galactic halo consists of two distinct populations: *i*) an inner, old, flattened one with a slight prograde rotation, and *ii*) an outer, younger, spherical one with no rotation. In both these studies stellar ages, or their proxies, were used to derive the main conclusions. ELS noted that the most extreme halo stars, by metallicity, have very elongated, highly elliptical orbits, and so must have formed during a very rapid Galactic collapse, over an interval of time short compared to a Galactic rotation period,  $\approx 2 \times 10^8$  years. On the other

Send offprint requests to: W.J. Schuster

\* Based on observations made with the Nordic Optical Telescope on La Palma, and on data from the European Southern Observatory ESO/ST-ECF Science Archive Facility (programmes 65.L-0507, 67.D-0086, 67.D-0439, 68.D-0094, 68.B-0475, 69.D-0679, 70.D-0474, 71.B-0529, 72.B-0585, 76.B-0133 and 77.B-0507).

\*\* Tables 1 and 4 are available in electronic form at <http://www.aanda.org>.

hand, SZ argued that the second parameter of the globular cluster horizontal branch morphologies is age, and observed that the outer globular clusters have a much wider range in color differences along their horizontal branches, implying a much wider range in ages,  $\gtrsim 10^9$  years, than for the inner globular clusters. (It has been widely discussed whether this second parameter is in fact the cluster age, but the most recent, more robust conclusions do support this conjecture, for example, Dotter et al. 2010.) Many later studies have seen the need to combine these two scenarios, ELS plus SZ, to more completely describe and understand the differing kinematics and ages of the inner and outer components of the halo (for example, Gilmore et al. 1989; Zinn 1993; Márquez & Schuster 1994; Jofré & Weiss 2011). However, the relative and absolute ages, from color-magnitude and color-metallicity diagrams for 1533 high-velocity and metal-poor stars in the solar neighborhood, have been interpreted consistently by Schuster et al. (2006) using the  $\Lambda$ CDM hierarchical-clustering scheme for the formation of galaxies without invoking these older scenarios of ELS and SZ.

The dichotomy of the Galactic halo has been supported by Carollo et al. (2007, 2010) from a study of space motions and metallicities of  $\simeq 17\,000$  stars within 4 kpc from the Sun in the SDSS survey. They find that the inner halo comprises stars with a peak metallicity at  $[\text{Fe}/\text{H}] \simeq -1.6$  whereas the outer halo stars distribute around  $[\text{Fe}/\text{H}] \simeq -2.2$  with a net retrograde rotation. Schönrich et al. (2011) have expressed doubts about these results, claiming the existence of large distance biases in Carollo et al. (2010), and questioning the existence of a separate outer, metal-poor halo component. Beers et al. (2011) have, however, made a new analysis of the SDSS stars with an improved luminosity classification, which supports the case for a dual halo. Also, an independent mapping of Milky Way structure based on color-magnitude diagram fitting of SEGUE photometric data by de Jong et al. (2010) provides clear evidence for a shift in the mean metallicity of the Milky Way’s stellar halo, from a peak of  $[\text{Fe}/\text{H}] \sim -1.6$  within 15 kpc to  $[\text{Fe}/\text{H}] \sim -2.2$  at larger Galactocentric distances, clearly supporting the Carollo et al. dual-halo view.

In addition, the inner halo itself may, however, consist of more than one population. In a study of a local sample of red giant, red horizontal branch, and RR Lyrae stars with  $[\text{Fe}/\text{H}] < -1.0$ , Morrison et al. (2009) find evidence of a highly flattened ( $c/a \sim 0.2$ ) halo component in addition to a moderately flattened ( $c/a \sim 0.6$ ) halo. This highly flattened population is mainly pressure supported; the mean prograde rotation is  $V_{\text{rot}} \simeq 45 \text{ km s}^{-1}$ , which distinguishes it from the thick disk that has  $V_{\text{rot}} \simeq 180 \text{ km s}^{-1}$ . Stars belonging to the moderately flattened halo have a mean rotation near zero and a clumpy distribution in energy and angular momentum, possible remnants of the early accretion of satellite galaxies (see review by Helmi, 2008).

Another study also makes use of halo stars from the SDSS survey to support a dual formation scenario for the Galactic halo, that of Jofré & Weiss (2011). They derive temperatures and metallicities for a sample of about 100,000 SDSS stars, and use a Sobel Kernel technique to detect the turn-offs of halo main sequence stars in the  $T_{\text{eff}}$  vs  $[\text{Fe}/\text{H}]$  diagram. They find “excellent” agreement with the  $(b-y)_{0,\text{TO}}$  versus  $[\text{Fe}/\text{H}]$  diagram of Schuster et al. (2006; Figure 9) from  $uvby-\beta$  photometry, and find clear evidence for a dominating halo population which formed 10–12 Gyr ago, with no gradient in age and metallicity, and with an

age scatter less than 2 Gyr. Jofré & Weiss (2011) also find a large number of halo stars bluer than these turn-offs for  $[\text{Fe}/\text{H}] \gtrsim -1.6$ , and suggest that these have come from smaller galaxies accreted later by the Milky Way. In essence they support the combined ELS plus SZ scenario of a rapid collapse of a proto-galactic cloud to form the inner halo, plus “collisions and mergers” to form the outer halo.

In addition to the study of halo field stars, the study of globular clusters has also shown clear evidence for a halo duality. A prime example of this is found in the paper by Marín-Franch et al. (2009) who obtained precise relative ages for 64 Galactic globular clusters from the deep, homogeneous photometric data of the ACS Survey of such globular clusters. They compared relative positions of the clusters’ main-sequence turnoffs, obtained formal precisions in the relative ages of 2–7%, and detected two clear components in the Galactic halo for metallicities  $[\text{Fe}/\text{H}] > -1.6$ . The older group shows an age dispersion of  $\approx 5\%$ , no age-metallicity relation, but with a clear galactocentric-distance-metallicity gradient. The younger group does show an age-metallicity relation with young clusters being more metal-rich than older ones. The age dispersion of the older group ( $\lesssim 0.8$  Gyr) corresponds to that expected for the free-fall time of a homogeneous sphere with the estimated mass and scale-length of the Milky Way’s dark matter halo, while the younger group apparently has formed by a different process over a time interval as long as  $\approx 6$  Gyr, which may be a lower limit to the actual range. Marín-Franch et al. (2009) point out that the age dispersion of the older cluster group “...is not in contradiction with the formation from the collapse of a single protosystem...” as in that model proposed by ELS, while “...it is very tempting to argue...” that the clusters of the younger group were associated with satellite galaxies that have been captured by the Milky Way over a significant time interval. Marín-Franch et al. (2009) indicate that the galactocentric-distance-metallicity gradient of the older group is not easily explained by the  $\Lambda$ CDM cosmological scenario, while it is also not easy to understand why all of the younger, accreted clusters should conform to the same age-metallicity relation, if indeed accreted with different dwarf galaxies, such as Sagittarius, Monoceros, Canis Major, and others.

Abundance ratios such as  $\alpha/\text{Fe}$ , are also important tracers of stellar populations and measures of difference in their ages. Thus, Freeman & Bland-Hawthorn (2002) discuss the possibility to use abundances (chemical tagging) to probe the satellite galaxies or proto-clouds from which the Galaxy was assembled according to the present paradigm of hierarchical structure formation in CDM cosmologies. The ratio  $[\alpha/\text{Fe}]$ , can be used as a ‘clock’ to probe the star formation rate for the chemical evolution of a Galactic region. since  $\alpha$  refers to typical alpha-capture elements like Mg, Si, Ca, and Ti, which are mainly produced during Type II SNe explosions of massive stars on a short time-scale ( $\sim 10^7$  years), whereas iron is also produced by Type Ia SNe on a much longer time scale ( $\sim 10^9$  years).

Stellar age is one of the parameters used to identify a stellar population, but is also that parameter most difficult to measure accurately and absolutely for individual field stars. Stellar ages have been used successfully to measure differences between the inner and outer halo, to compare the thick disk and halo, and to interpret the Galactic halo in terms of WMAP and  $\Lambda$ CDM models (Nissen & Schuster 1991; Márquez & Schuster 1994; Schuster et al. 2006; Jofré

& Weiss 2011.) For old field stars it is difficult to obtain the ages much better than 20% (Gustafsson & Mizuno-Wiedner 2001), but relative ages within an ensemble of stars can be more precise, perhaps better than 10%, and the mean relative ages between stellar populations provide the best results considering the large number of stars, and assuming that one can obtain fairly pure samples and can control systematic effects as a function of  $T_{\text{eff}}$  and metallicity.

The integration of stellar orbits within realistic Galactic mass models has also provided information useful for characterizing and comparing stellar components (Allen et al. 1991; Schuster & Allen 1997); stellar ages have been combined with orbital integrations to study a possible difference in age between the inner and outer halo (Márquez & Schuster 1994). Non-axisymmetric, observationally constrained, Galactic potentials, with and without bars and/or spiral arms, have been used to study orbital characteristics and chaos, and the destruction rates for Galactic globular clusters (Pichardo et al. 2004; Allen et al. 2006, 2008).

Additional evidence for the existence of two distinct halo populations has recently been obtained by Nissen & Schuster (2010, 2011) (Papers I and II) from a study of chemical abundances of stars in the solar neighborhood. These halo stars were selected from Strömgren photometry (Schuster et al. 2006) to have effective temperatures  $5200 < T_{\text{eff}} < 6300$  K, metallicities  $-1.6 < [\text{Fe}/\text{H}] < -0.4$ , and total space velocities with respect to the local standard of rest (LSR)  $V_T \geq 180 \text{ km s}^{-1}$ . This means that they belong to the metal-rich end of the halo metallicity distribution; halo stars with  $[\text{Fe}/\text{H}] < -1.6$  are not represented in the sample. In addition spectroscopic data for 16 thick-disk stars were obtained, analyzed, and used for comparison. The two halo groups are clearly separated in the  $[\text{Mg}/\text{Fe}]$  versus  $[\text{Fe}/\text{H}]$  or  $[\alpha/\text{Fe}]$  versus  $[\text{Fe}/\text{H}]$  diagrams, where  $\alpha$  represents the average abundance for Mg, Si, Ca, and Ti. But also differences between these two halo groups have been noted for the abundances  $[\text{Na}/\text{Fe}]$ ,  $[\text{Ni}/\text{Fe}]$ ,  $[\text{Cu}/\text{Fe}]$ ,  $[\text{Zn}/\text{Fe}]$ , and  $[\text{Ba}/\text{Y}]$ . These two halo components, ‘high-alpha’ and ‘low-alpha’, have been interpreted in terms of high and low star formation rates, respectively, so that the first group obtained chemical enrichment from Type II supernovae (SNeII) only, while the ‘low-alpha’ component received chemical enrichment from both SNeII and SNeIa; the latter produce much iron diluting the overabundance of some products from the SNeII. Similarities of the ‘low-alpha’ kinematics to the globular cluster  $\omega$  Cen prompted us to compare their chemical abundances, but only a partial correspondence, for  $[\text{Ni}/\text{Fe}]$  and  $[\text{Cu}/\text{Fe}]$ , was obtained;  $\omega$  Cen is lacking in stars showing the SNeIa contamination characteristic of the ‘low-alpha’ halo stars. This dual halo result was compared to the chemical abundances for various dSph and dIrr galaxies in the literature, as well as to several models used to produce Galactic halos.

In this paper, stellar ages are obtained from the  $Y^2$  isochrones (Yi et al. 2001, 2003; Kim et al. 2002; and Demarque et al. 2004), and orbital parameters from integrations using both the axisymmetric and non-axisymmetric, observationally-constrained, Galactic mass models of Allen & Santillán (1991), and Pichardo et al. (2003, 2004). These ages and orbital parameters are used to better understand the differences between these ‘high-alpha’ and ‘low-alpha’ halo stars, and to determine more clearly how this dual halo has been formed, by comparing to three different sets of models, or scenarios, in the literature: the classic ELS-plus-

SZ scenario, the accretion-plus-accretion (dual-accretion) models of Font et al. (2006a) and of Robertson et al. (2005), and the *insitu*-plus-accretion models of Zolotov et al. (2009, 2010) and of Purcell et al. (2010).

In Sect. 2 the derivation of the stellar parameters ( $T_{\text{eff}}$  and  $\log g$ ) and of their errors is described; in Sect. 3 the calculation of the stellar ages for the ‘high-alpha’, ‘low-alpha’, and thick-disk stars, and the mean ages for these different groups are presented; in Sect. 4, the integration of the Galactic orbits is described, and several graphs showing orbital parameters versus other orbital parameters, or versus chemical abundances, are given; finally Sect. 5 sums it all together with a discussion of the results and the main conclusions, plus epilogue.

## 2. Stellar parameters and abundances

As described in Sect. 3, stellar ages are determined from isochrones in the  $\log g$ - $\log T_{\text{eff}}$  plane. The precision of relative ages is therefore closely related to the errors in the determination of effective temperature and surface gravity. In this section, we summarize how these two parameters were determined in Papers I and II and check the errors by comparing spectroscopic and photometric values for stars that are unlikely to be affected by interstellar reddening.

### 2.1. Chemical abundances

The chemical abundances of our program stars are based on equivalent widths (EWs) measured from high-resolution, high-S/N spectra and analyzed differentially with respect to two bright thick-disk stars, HD 22879 and HD 76932. They have distances of 26 and 21 pc, respectively, according to their Hipparcos parallaxes (van Leeuwen 2007). Hence, the two stars are so close that their colors are not affected by interstellar reddening. Effective temperatures were determined from  $b-y$  and  $V-K$  using calibrations derived by Ramírez & Meléndez (2005), who applied the infrared flux method (IRFM) to determine  $T_{\text{eff}}$ .  $V$  magnitudes and  $b-y$  indices were taken from Schuster et al. (2006) and  $K$  magnitudes from the 2MASS catalogue (Skrutskie et al. 2006). The resulting values of  $T_{\text{eff}}$  are given in Table 1 (online). As seen, there is excellent agreement between the temperatures from  $b-y$  and  $V-K$ ; the difference is less than 15 K for both stars.

The surface gravities of HD 22879 and HD 76932 given in Table 1 were determined from the fundamental relation

$$\log \frac{g}{g_{\odot}} = \log \frac{\mathcal{M}}{\mathcal{M}_{\odot}} + 4 \log \frac{T_{\text{eff}}}{T_{\text{eff},\odot}} + 0.4(M_{\text{bol}} - M_{\text{bol},\odot}) \quad (1)$$

where  $\mathcal{M}$  is the mass of the star and  $M_{\text{bol}}$  the absolute bolometric magnitude. The Hipparcos parallax was used to derive  $M_V$  and the bolometric correction adopted from Alonso et al. (1995). The stellar mass was obtained by interpolating in the  $M_V$ - $\log T_{\text{eff}}$  diagram between the evolutionary tracks of VandenBerg et al. (2000). Due to the small error of the Hipparcos parallaxes of HD 22879 and HD 76932,  $\sigma(\pi)/\pi < 0.015$  (van Leeuwen 2007), the estimated error of  $\log g$  is only 0.03 dex for both stars.

With the so derived values of  $T_{\text{eff}}$  and  $\log g$ , chemical abundances relative to the Sun were derived for the two standard stars using a subset of spectral lines for which the equivalent widths could be measured reliably in the solar

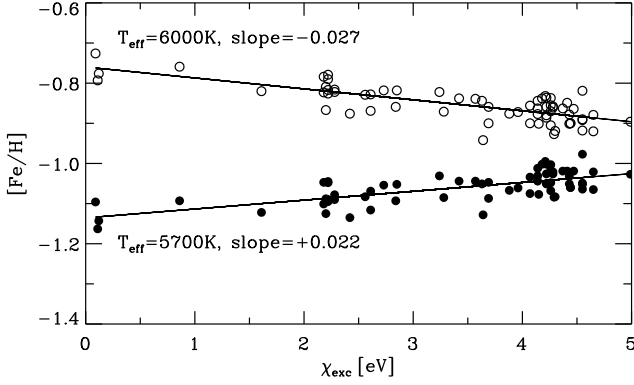


**Fig. 1.**  $[\text{Fe}/\text{H}]$  values derived from Fe I lines with  $\text{EW} < 50 \text{ m}\text{\AA}$  in the spectrum of G 56-30 as a function of excitation potential for the lower energy level. The open circles refer to an effective temperature of 6000 K for the model atmosphere used and the filled circles to a model with  $T_{\text{eff}} = 5700 \text{ K}$ .

flux spectrum (Kurucz et al. 1984). Adopting these abundances, an ‘inverted’ analysis led to the determination of  $gf$ -values for all lines. The derived  $gf$ -values for HD 22879 and HD 76932 agree within  $\pm 0.03$  dex for the large majority of lines; hence, for each line, the mean value of  $gf$  (see Table 3 in Paper II) were adopted and used for an LTE analysis of all program stars based on MARCS model atmospheres from Gustafsson et al. (2008). This method ensures that high-precision differential abundances relative to the two standard stars are obtained. Further details about spectral lines and line-broadening mechanisms included are given in Papers I and II.

## 2.2. Effective temperature

For the majority of the 94 program stars, interstellar NaD lines are clearly seen in their spectra (see Tables 1 and 2 in Paper I). The colors of these stars are therefore probably affected by interstellar reddening. Although, the reddening excess may be estimated via the  $\text{H}\beta$  index (Schuster & Nissen 1989) or from the strength of the NaD lines (Alves-Brito et al. 2010), the precision of  $T_{\text{eff}}$  derived from colors will not be as high as in the case of unreddened stars. Therefore, we preferred to determine effective temperatures spectroscopically, i.e. by requiring that the Fe abundances derived from Fe I lines do not depend systematically on excitation potential.

Fig. 1 illustrates the method in the case of G 56-30. By interpolating between the slopes for  $T_{\text{eff}} = 5700 \text{ K}$  and  $6000 \text{ K}$ , an effective temperature of  $5830 \text{ K}$  is derived for this star. As the Fe I lines are also applied to determine the microturbulence,  $\xi_{\text{turb}}$ , by minimizing the dependence of  $[\text{Fe}/\text{H}]$  on equivalent width, only lines with  $\text{EW} < 50 \text{ m}\text{\AA}$  were used to estimate  $T_{\text{eff}}$ , whereas  $\xi_{\text{turb}}$  is based only on Fe I lines with  $\chi_{\text{exc}} > 3.0 \text{ eV}$ . In this way, the determination of  $T_{\text{eff}}$  and  $\xi_{\text{turb}}$  is to some extent decoupled, although it is necessary to iterate in order to obtain consistent values of  $T_{\text{eff}}$  and  $\xi_{\text{turb}}$ . From the error of the excitation slopes, we estimate that the  $1\text{-}\sigma$  statistical error of  $T_{\text{eff}}$  is on the order of 20 to 30 K depending on the number of  $[\text{Fe}/\text{H}]$  lines available.

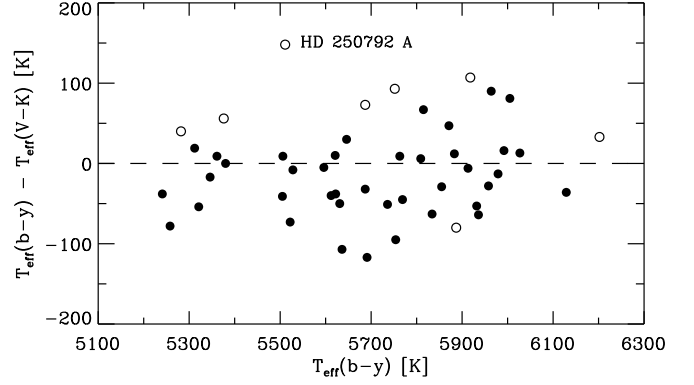


**Fig. 2.** The difference of effective temperatures as determined from the photometric colors  $b-y$  and  $V-K$  for stars with no detectable interstellar NaD lines. Known binary stars are shown with open circles.

A check of the estimated precision of the effective temperatures as derived from the excitation balance of Fe I lines may be obtained by comparing with temperatures derived from  $b-y$  and  $V-K$  for stars having no detectable interstellar NaD lines, i.e.  $\text{EW} \lesssim 3 \text{ m}\text{\AA}$  for UVES spectra and  $\text{EW} \lesssim 5 \text{ m}\text{\AA}$  for FIES spectra. Such stars are unlikely to be affected by interstellar reddening (e.g. Nissen 1994; Alves-Brito et al. 2010).  $T_{\text{eff}}$  values as derived from  $b-y$  and  $V-K$  using the Ramírez & Meléndez (2005) calibrations and the same sources of photometry as in the case of the standard stars are given in Table 1 together with the spectroscopic values of  $T_{\text{eff}}$ . As listed in the last column of the table, four of the stars are single-lined spectroscopic binaries and another four stars have close companions, which are probably affecting the color indices and hence the derived values of  $T_{\text{eff}}$ .

Fig. 2 shows a comparison of the effective temperatures derived from  $b-y$  and  $V-K$ . As seen,  $T_{\text{eff}}(b-y)$  is larger than  $T_{\text{eff}}(V-K)$  for seven of the eight binary stars. This can be explained if the secondary component is a red, low-mass star affecting in particular the infrared  $K$  magnitude. An exception is HD 219617 for which the two components have similar magnitudes and nearly identical spectra. (Takeda & Takada-Hidai 2011).

There are no signatures of a secondary component in the spectra of the binary stars, except for the spectrum of HD 250792 A, which has unusually strong and slightly shifted MgH lines around  $5100 \text{ \AA}$  probably arising from a cool component. HD 250792 A is the binary star that shows the largest difference between  $T_{\text{eff}}(b-y)$  and  $T_{\text{eff}}(V-K)$ , i.e.  $148 \text{ K}$ .

Excluding the binary stars, the rms scatter of the difference  $T_{\text{eff}}(b-y) - T_{\text{eff}}(V-K)$  is  $50 \text{ K}$ . This suggests that each of the two temperatures are determined with a precision of  $\sim 35 \text{ K}$ , and that the precision of the mean photometric temperature,  $T_{\text{eff}}(\text{phot}) = 1/2 (T_{\text{eff}}(b-y) + T_{\text{eff}}(V-K))$ , is about  $25 \text{ K}$  for single stars. A comparison of this photometric temperature with the spectroscopic value of  $T_{\text{eff}}$  is shown in Fig. 3 (excluding the two standard stars for which the two sets of temperatures agree by definition). As seen, the agreement is excellent. Without the binary stars, the rms scatter of the difference is  $33 \text{ K}$ . Adopting an error of  $25 \text{ K}$  in  $T_{\text{eff}}(\text{phot})$  this corresponds to an error of  $22 \text{ K}$  of  $T_{\text{eff}}(\text{spec})$ . If the binary stars are included, the rms scatter

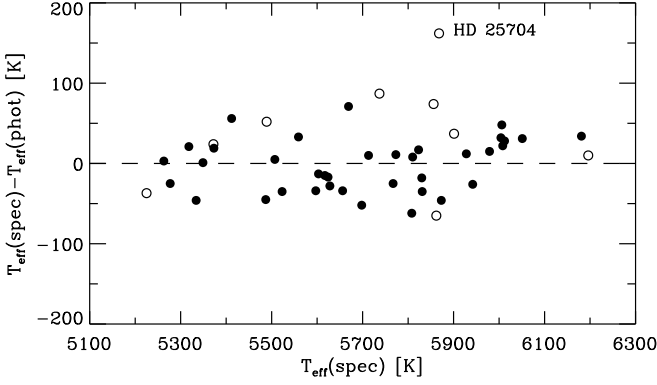


**Fig. 3.** The difference of effective temperatures determined from the excitation balance of Fe I lines and from the photometric colors  $b-y$  and  $V-K$  for stars without detectable interstellar NaD lines. Known binary stars are shown with open circles.

of the difference between  $T_{\text{eff}}(\text{spec})$  and  $T_{\text{eff}}(\text{phot})$  increases to 44 K with a large contribution to the scatter coming from HD 25704.

We suggest that binarity is affecting  $T_{\text{eff}}(\text{phot})$  more than it is affecting  $T_{\text{eff}}(\text{spec})$ . Out of the 94 program stars, eight stars are designated as SB1 in the SIMBAD database and five stars have close companions according to the Hipparcos catalogue, but only in two cases (HD 250792 A and HD 163810), there are signs of a secondary spectrum in our high-resolution spectra, i.e. unusually strong and asymmetric MgH lines. For these two stars,  $T_{\text{eff}}$  for the primary component is probably slightly higher than the derived  $T_{\text{eff}}(\text{spec})$ .

On the basis of these comparisons, we adopt  $\pm 30$  K as the 1-sigma statistical error for the effective temperatures used in the age determinations. The systematic error may, however be larger. Our  $T_{\text{eff}}$  values refer to the IRFM temperatures of Ramírez & Meléndez (2005), but recently Casagrande et al. (2010) have carefully revisited the IRFM method for dwarf and subgiant stars finding a systematic offset of +100 K in  $T_{\text{eff}}$  relative to the Ramírez & Meléndez values for stars with  $[\text{Fe}/\text{H}] > -2.0$  and  $4800 < T_{\text{eff}} < 6200$  K (see Fig. 5 in Casagrande et al. 2010). The difference mainly stems from the infrared absolute flux calibrations applied; Casagrande et al. have taken advantage of accurate HST spectrophotometry of Vega by Bohlin (2007). Furthermore, they have validated the new  $T_{\text{eff}}$  scale by interferometric angular diameter measurements and solar twins, i.e. stars having high-resolution spectra indistinguishable from the solar flux spectrum and therefore  $T_{\text{eff}}$  close to 5780 K. Thus, it seems that the  $T_{\text{eff}}$  values published in Papers I and II are systematically too low by  $\sim 100$  K; as mentioned in Sect. 3 we have corrected for this in the age determinations.

It should be noted that an increase of 100 K in  $T_{\text{eff}}$  has only a small effect on the abundances derived. This is due to the fact that  $[\text{Fe}/\text{H}]$  is determined from Fe II lines and that the abundance ratios are based on lines corresponding to the same ionization stage of the elements. The correction of  $[\text{Fe}/\text{H}]$  is about  $-0.03$  dex at  $T_{\text{eff}} = 5400$  K and  $+0.01$  dex at  $T_{\text{eff}} = 6100$  K, whereas the correction of  $[\alpha/\text{Fe}]$  is approximately constant at  $-0.01$  dex. These corrections

have a very small effect on the derived ages and may be neglected.

### 2.3. Surface gravity

Several of the program stars are missing Hipparcos parallaxes and in other cases, the relative error of the parallaxes is too large to allow a precise determination of  $\log g$  from Eq. (1). Therefore, we have preferred to determine a spectroscopic value of  $\log g$  from the requirement that the Fe abundance derived from Fe I and Fe II lines should have the same difference as in the case of the standard stars, i.e.  $[\text{Fe}/\text{H}]_{\text{II}} - [\text{Fe}/\text{H}]_{\text{I}} = 0.075$ . This difference is probably due to a departure from LTE in the ionization balance of Fe. It is therefore implicitly assumed that this non-LTE deviation does not change significantly as a function of  $T_{\text{eff}}$  or  $[\text{Fe}/\text{H}]$  for the sample of stars considered.

The strength of Fe I lines is nearly independent of  $\log g$ , whereas the Fe abundance derived from Fe II lines increases by about 0.04 dex if  $\log g$  of the model atmosphere is increased by 0.1 dex. Since we have about 90 Fe I and 15 Fe II lines available, the difference  $[\text{Fe}/\text{H}]_{\text{II}} - [\text{Fe}/\text{H}]_{\text{I}}$  can be determined to a precision of about 0.02 dex. This corresponds then to a precision of 0.05 dex in the determination of  $\log g$ . Again, it should be emphasized that this estimate refers to differential values of  $\log g$  relative to the gravities of the two standard stars.

As a test of the gravities derived from the ionization balance of Fe lines, Fig. 4 compares  $\log g(\text{spec})$  with the gravity derived from Eq. (1) using Hipparcos parallaxes to determine the distance and hence the absolute magnitude. To avoid effects from reddening only stars without detectable interstellar NaD lines are included in the comparison, i.e. the sample listed in Table 1. The derived values of  $\log g(\text{HIP})$  and their errors (with the main contribution coming from the error of the parallax) are given in Col. 8. As seen, four stars have no Hipparcos parallax and one star (G 46-31) has a very large error in  $\log g(\text{HIP})$ . The rest (except the two standard stars, for which the two sets of gravities agree by definition) are plotted in Fig. 4. The error bars on  $\Delta \log g = \log g(\text{spec}) - \log g(\text{HIP})$  are calculated as a quadratic addition of the errors of  $\log g(\text{HIP})$  and  $\log g(\text{spec})$ , the latter assumed to be  $\pm 0.05$  dex.

Fig. 4 shows a very satisfactory agreement between  $\log g(\text{spec})$  and  $\log g(\text{HIP})$ . The reduced chi-square  $\chi^2_{\text{red}} = 1/N \sum (\Delta \log g_i / \sigma_i)^2$  is 0.94, and there is no significant offset of the binary stars<sup>1</sup>. This suggests that  $\pm 0.05$  dex is a realistic estimate for the error of  $\log g(\text{spec})$ .

As discussed in Sect. 2.2, the new IRFM temperatures by Casagrande et al. (2010) suggest that the  $T_{\text{eff}}$  values in Papers I and II are systematically too low by 100 K. This change of the temperature scale has a small systematic effect on the estimated gravities; due to the  $T_{\text{eff}}$  term in Eq. (1), the  $\log g$  values of the standard stars increase by 0.03 dex.

<sup>1</sup> In deriving  $\log g(\text{HIP})$  for HD 219617 we have used the visual magnitude,  $V = 8.77$  of the primary component as measured by Takeda & Takada-Hidai (2011). For the other three close binaries we have estimated the magnitude of the primary component by using the magnitude difference given in Table 1.

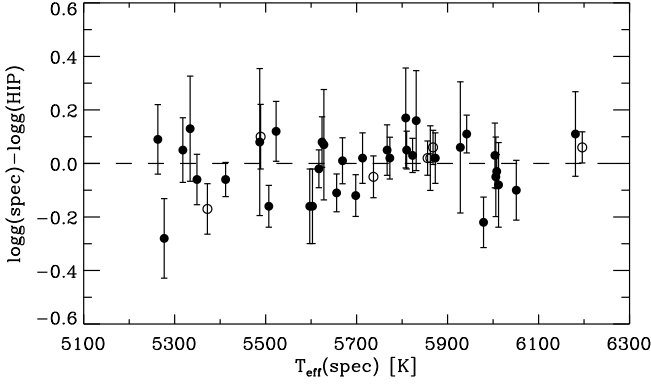


**Fig. 4.** The difference of logarithmic surface gravity derived from the ionization balance of Fe lines and from Eq. (1) using Hipparcos parallaxes to determine the absolute bolometric magnitude. Only stars with no detectable interstellar NaD lines are included, and known binaries are shown with open circles.

### 3. Ages

The relative ages of this study have been determined using the  $Y^2$  isochrones of Yi et al. (2001, 2003), Kim et al. (2002), and Demarque et al. (2004), which allow interpolation to the exact values of  $[\text{Fe}/\text{H}]$  and  $[\alpha/\text{Fe}]$  as determined by our spectroscopic measures.  $[\text{Fe}/\text{H}]$  represents the mean metallicity of the star, and  $[\alpha/\text{Fe}]$  the deviation of the alpha elements from this mean. For each of our halo and thick-disk stars, an isochrone set in the  $\log g$ - $\log T_{\text{eff}}$  plane has been interpolated to the exact spectroscopic values of  $[\text{Fe}/\text{H}]$  and  $[\alpha/\text{Fe}]$  for that star.

However, before the final relative ages could be derived, problems relating to possible systematic effects had to be resolved. As discussed in Sect. 2.2, the recent work of Casagrande et al. (2010) suggests that a correction of +100 K should be applied to the spectroscopic temperatures in Papers I and II before comparing each star to its corresponding isochrone set. This systematic correction lowers the resulting ages to values more in line with the WMAP age for the Universe ( $13.75 \pm 0.13$  Gyr; Jarosik et al. 2011, Larson et al. 2011). Also, Jofré & Weiss 2011, in their study of the turn-offs of halo main sequence stars from the SDSS survey, show that gravitational settling of heavy elements (diffusion) is necessary for the isochrone models to produce ages compatible with the age of the Universe; models without this diffusion can produce ages as much as 4 Gyr larger. The  $Y^2$  isochrones used in the present paper do make use of such gravitational settling.

In addition, our 13 coolest stars,  $T_{\text{eff}} < 5600$  K, show systematic vertical offsets (in  $\log g$ ) with respect to the isochrones in the  $\log g$ - $\log T_{\text{eff}}$  plane. Such cool stars should be little evolved from their corresponding ZAMS isochrones, even for the total age of the Universe, and so these 13 stars (twelve halo and one thick-disk) have been fit to isochrones with ages of 13 Gyr at their corresponding values of  $[\text{Fe}/\text{H}]$  and  $[\alpha/\text{Fe}]$  and with the above correction of +100 K to the stars'  $T_{\text{eff}}$  values. Such fitting derives a correction of  $\Delta \log g = -0.127$  dex, which has been applied to all  $Y^2$  isochrones used for our age analyses.

A small part of this gravity correction stems from the need for a systematic change of +0.03 dex in the stellar

$\log g$  values caused by the +100 K increase in  $T_{\text{eff}}$  (Eq. 1). The remaining part seems to be due to a systematic error in  $\log g$  of the isochrones. A corresponding offset between isochrones and unevolved stars with metallicities in the range  $-1.0 < [\text{Fe}/\text{H}] < -0.5$  is present in the  $M_{\text{bol}}$ - $\log T_{\text{eff}}$  diagram (Lebreton 2000) even if the new  $T_{\text{eff}}$  scale of Casagrande et al. (2010) is adopted (Casagrande et al. 2011, Fig. 12).

The  $\log g$  offset of the isochrones relative to the unevolved stars may be related to the mixing length parameter,  $l/H_p$ , used in modeling the upper convection zone. The stellar radius and hence  $\log g$  depends on its value. Usually the mixing length parameter is assumed to be independent of  $[\text{Fe}/\text{H}]$  and is determined by fitting a model of the Sun to the solar parameters, e.g.  $l/H_p = 1.74$  in the case of the  $Y^2$  isochrones. If instead  $l/H_p$  decreases to about 1.2 at  $[\text{Fe}/\text{H}] = -1$ , the  $\log g$  offset of the isochrones would go away according to the calculations of Vandenberg (1983). Such a change of  $l/H_p$  would also decrease  $T_{\text{eff}}$  of the isochrones in the turnoff region and hence decrease the derived ages of our stars by 2–3 Gyr. For this reason, the absolute ages of our stars are rather uncertain, but the relative ages of the stars at a given metallicity are insensitive to the mixing length parameter and should be quite precise.

In Figs. 5 and 6 are shown groups of ‘high-alpha’ halo, ‘low-alpha’ halo, and thick-disk stars over the metallicity ranges of  $-1.20 < [\text{Fe}/\text{H}] < -0.975$  and  $-0.975 < [\text{Fe}/\text{H}] < -0.775$ , respectively. The  $Y^2$  isochrones have been interpolated to the corresponding mean values of  $[\text{Fe}/\text{H}] = -1.0875$  and  $[\alpha/\text{Fe}] = +0.250$ , and  $[\text{Fe}/\text{H}] = -0.875$  and  $[\alpha/\text{Fe}] = +0.215$ , respectively. The full (red) circles show the ‘low-alpha’ halo stars, the open (blue) circles the ‘high-alpha’ halo, and the (green) pluses the thick-disk. The sizes of the error bars are those derived above in Subsection 3.6:  $\pm 0.05$  dex in  $\log g$  and  $\pm 0.0022$  in  $\log T_{\text{eff}}$  (corresponding to  $\pm 30$  K in  $T_{\text{eff}}$ ). The correction +100 K has been added to the spectroscopic  $T_{\text{eff}}$  values of the stars, and the isochrones shifted by  $\Delta \log g = -0.127$  dex. Both figures show clear evidence for  $\langle \text{Age} \rangle_{\text{low-alpha}} < \langle \text{Age} \rangle_{\text{high-alpha}}$ , and both suggest a sequence:  $\langle \text{Age} \rangle_{\text{low-alpha}} < \langle \text{Age} \rangle_{\text{thick-disk}} < \langle \text{Age} \rangle_{\text{high-alpha}}$ .

In deriving ages for individual stars, we have also set the limits  $3.8 < \log g < 4.4$  for those stars which will have their ages estimated. Outside these limits the isochrone spacing is too small to provide a good precision for these age determinations.

In Table 2, mean, weighted ages are given for the four components: ‘high-alpha’ halo, ‘low-alpha’ halo, thick-disk, and ‘high-alpha’ halo plus thick-disk, and for five metallicity ranges from  $-1.40 < [\text{Fe}/\text{H}] < -1.20$  to  $-0.575 < [\text{Fe}/\text{H}] < -0.40$ . For these weighted averages each star has been plotted in a separate  $\log g$ - $\log T_{\text{eff}}$  diagram with the  $Y^2$  isochrones interpolated exactly to that star’s  $[\text{Fe}/\text{H}]$  and  $[\alpha/\text{Fe}]$  values. The age of each star has been interpolated in its corresponding  $\log g$ - $\log T_{\text{eff}}$  diagram, as well as the ages at each of the corners of the error box constructed from the error bars. Each of these ‘corner’ ages provides an age error estimate for that star, and the four of these have been averaged for the final error estimate of that star’s age,  $\sigma_*$ . Then the weight for that star’s age has been taken as:  $1/\sigma_*^2$ . In Table 2 these weighted ages are given for each of the Galactic components, over the five metallicity ranges, as well as the weighted standard deviations, and the number of stars in each group.

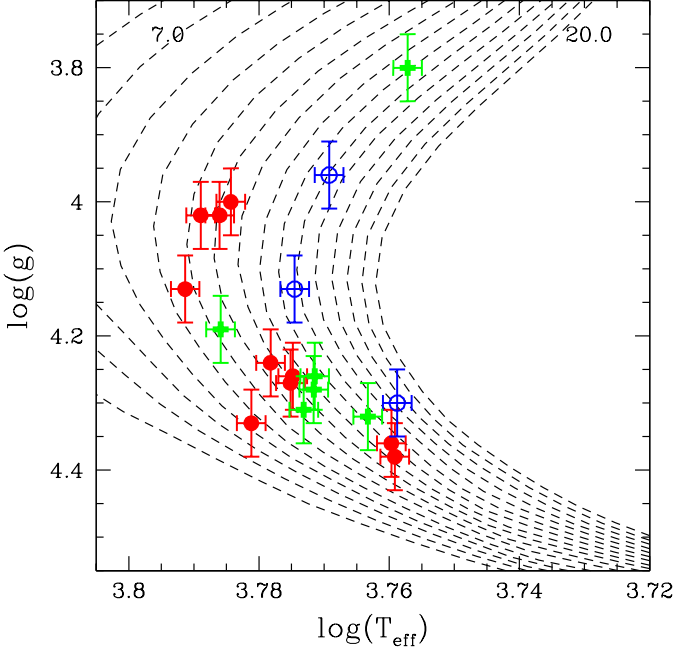


**Fig. 5.** The  $\log g$ - $\log T_{\text{eff}}$  diagram for stars with  $-1.20 < [\text{Fe}/\text{H}] < -0.975$ .  $Y^2$  isochrones corresponding to  $[\text{Fe}/\text{H}] = -1.0875$  and  $[\alpha/\text{Fe}] = +0.25$  are over-plotted in steps of 1 Gyr from 5 to 20 Gyr. The full (red) circles show the ‘low-alpha’ halo stars, the open (blue) circles the ‘high-alpha’ halo, and the (green) pluses the thick-disk.

The results of this Table 2 are concordant with those from Figs. 5 and 6, showing clearly that  $\langle \text{Age} \rangle_{\text{low-alpha}} < \langle \text{Age} \rangle_{\text{high-alpha}}$ , and suggesting again a sequence:  $\langle \text{Age} \rangle_{\text{low-alpha}} < \langle \text{Age} \rangle_{\text{thick-disk}} < \langle \text{Age} \rangle_{\text{high-alpha}}$ .

#### 4. Orbital parameters

The calculation of stellar space velocities is described in Paper I. In summary, proper motions are acquired from the Tycho-2 catalogue (Høg et al. 2000) for the large majority of stars, radial velocities from our own spectral analyses, and distances from Hipparcos parallaxes (van Leeuwen 2007), or from the photometric absolute magnitude calibration by Schuster et al. (2004, 2006). The resulting values of the velocity components  $U_{\text{LSR}}$ ,  $V_{\text{LSR}}$ ,  $W_{\text{LSR}}$  with respect to the LSR are given in Tables 3 and 4 in Paper I. The typical errors of these components are  $(\pm 12, \pm 16, \pm 9)$  km s $^{-1}$  with the principal contribution coming from the error in the distances.

In Fig. 7 we have repeated the Toomre diagram from Paper I for thick-disk and halo stars with  $-1.4 < [\text{Fe}/\text{H}] < -0.4$ . For this range, it is possible to make a clear classification into the ‘high- $\alpha$ ’ and ‘low- $\alpha$ ’ populations from the  $[\alpha/\text{Fe}]$ - $[\text{Fe}/\text{H}]$  diagram. In the metallicity range  $-1.6 < [\text{Fe}/\text{H}] < -1.4$ , the two halo populations tend to merge in  $[\alpha/\text{Fe}]$ , and the classification is less clear. For this reason, all following figures with orbital parameters are confined to stars having  $[\text{Fe}/\text{H}] > -1.4$ , i.e. 35 ‘high- $\alpha$ ’, 32 ‘low- $\alpha$ ’, and 16 thick-disk stars.

With these kinematic data, Galactic orbits of the stars were computed backward in time 1, 2, and 5 Gyr in a detailed semi-analytic model of the Milky Way potential,

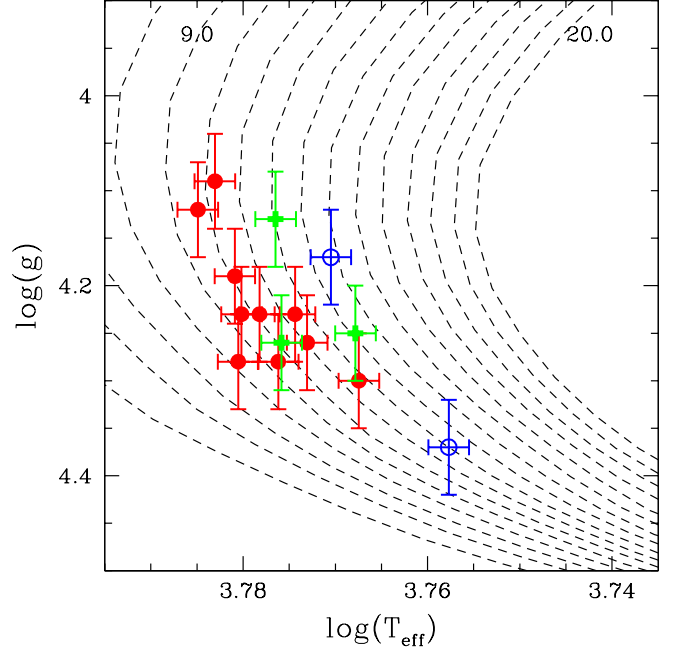


**Fig. 6.** The  $\log g$ - $\log T_{\text{eff}}$  diagram for stars with  $-0.975 < [\text{Fe}/\text{H}] < -0.775$ .  $Y^2$  isochrones corresponding to  $[\text{Fe}/\text{H}] = -0.875$  and  $[\alpha/\text{Fe}] = +0.215$  are over-plotted in steps of 1 Gyr from 5 to 20 Gyr. The symbols as in Fig. 5.

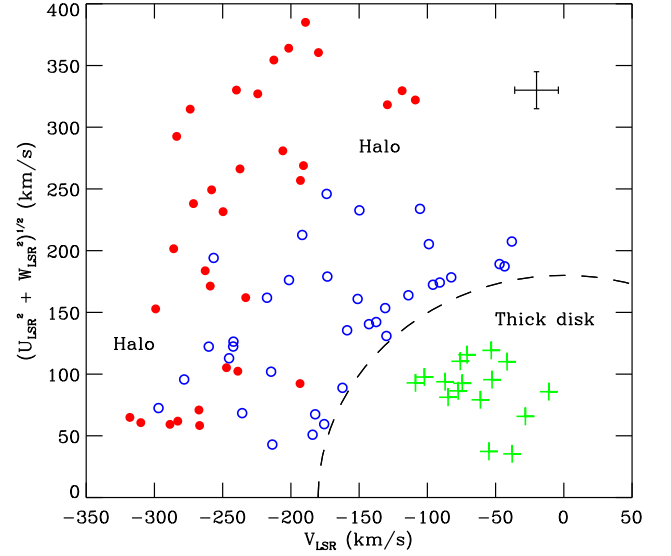


**Fig. 7.** Toomre diagram for ‘high- $\alpha$ ’ halo, ‘low- $\alpha$ ’ halo, and thick-disk stars with  $[\text{Fe}/\text{H}] > -1.4$ . The same symbols as in Fig. 5 are used. The long-dashed line corresponds to  $V_{\text{total}} = 180$  km s $^{-1}$ .

which has been constrained to fit numerous observations of the Galactic bar and spiral arms. The Bulirsch-Stoer algorithm given by Press et al. (1992) was used in the computations of the Galactic stellar orbits. Orbital parameters such as  $r_{\text{max}}$ ,  $z_{\text{max}}$ , and  $e_{\text{max}}$  have been derived, where these are the maximum distances from the Galactic center and from the Galactic disk, and the maximum orbital eccentricity obtained during the orbital excursions of these inte-

**Table 2.** Average, weighted ages (in Gyr) with mean errors and the number of stars, for five ranges in  $[\text{Fe}/\text{H}]$  and for the four components mentioned in the text: ‘high-alpha’ halo, ‘low-alpha’ halo, thick-disk, and ‘high-alpha’ halo plus thick-disk

Group / $[\text{Fe}/\text{H}]$ :	[−1.40, −1.20]			[−1.20, −0.975]			[−0.975, −0.775]			[−0.775, −0.575]			[−0.575, −0.40]		
	$\langle \text{Age} \rangle$	$\sigma$	N	$\langle \text{Age} \rangle$	$\sigma$	N	$\langle \text{Age} \rangle$	$\sigma$	N	$\langle \text{Age} \rangle$	$\sigma$	N	$\langle \text{Age} \rangle$	$\sigma$	N
‘low-alpha’ halo	11.14	$\pm 0.42$	5	10.78	$\pm 0.24$	10	10.46	$\pm 0.32$	10	...	...	...	...	...	...
‘high-alpha’ halo	11.70	$\pm 0.51$	4	14.47	$\pm 0.62$	3	12.66	$\pm 0.67$	2	11.35	$\pm 0.33$	13	9.07	$\pm 0.43$	6
thick-disk	11.60	$\pm 0.80$	1	12.01	$\pm 0.54$	6	11.56	$\pm 0.50$	3	10.46	$\pm 0.58$	3	...	...	...
‘high-alpha’ + thick-disk	11.67	$\pm 0.43$	5	13.07	$\pm 0.41$	9	11.95	$\pm 0.40$	5	11.12	$\pm 0.29$	16	9.07	$\pm 0.43$	6

grations, respectively. The orbital integrations were carried out with both symmetrical and non-symmetrical models. The more complicated and more realistic non-symmetrical model includes an axisymmetric background potential as well as non-axisymmetric Galactic components: bar and spiral arms. The axisymmetric model used, with bulge, disk, and dark halo components, is the Galactic model of Allen & Santillán (1991), scaled to give a rotational velocity of  $254 \text{ km s}^{-1}$  at the solar position, a value recently found by Reid et al. (2009). The Sun-Galactic center distance has been taken as  $R_0 = 8.5 \text{ kpc}$ , which is within the range found by Reid et al. (2009) ( $R_0 = 8.6 \pm 0.6 \text{ kpc}$ ). In the Galactic potential the original scaled disk and bulge components of the axisymmetric model are modified in order to introduce the bar and spiral arms, keeping the same original scaled mass. All the mass in the original scaled spherical bulge is now used to build the bar, and a fraction of the mass of the original scaled disk is employed to build the spiral arms. Thus the remaining axisymmetric components are just the diminished disk and the original scaled spherical dark halo.

The Galactic three-dimensional potential for the spiral arms are modeled following Pichardo et al. (2003). The spiral arms consist of a superposition of inhomogeneous oblate spheroids, which can be adjustable to better represent the available observations of the Galactic spiral arms. The spiral arms in the model trace the locus found by Drimmel & Spergel (2001), from K-band observations. The total mass of these arms is 3% of the mass of the scaled axisymmetric disk. With this mass the mean ratio of the radial force due to the arms to that of the axisymmetric background is around 10%, in agreement with the estimations by Patsis et al. (1991) for Milky Way-type galaxies. Also, the parameter  $Q_t$ , which is the ratio of the maximum azimuthal force of the spiral arms at a given Galactocentric distance on the Galactic plane, to the radial axisymmetric force at that distance (Sanders & Tubbs 1980; Combes & Sanders 1981) reaches a maximum value  $(Q_t)_{\text{max}} = Q_s = 0.12$ , which is appropriate for a Hubble-type galaxy like the Milky Way (Buta et al. 2004; Buta et al. 2005). The self-consistency of the spiral arms is tested through the reinforcement of the spiral potential by the stellar orbits; see details in Patsis et al. (1991) and Pichardo et al. (2003). In our computations,  $20 \text{ km s}^{-1} \text{ kpc}^{-1}$  has been used for the pattern speed of the spiral arms (Martos et al. 2004).

For the Galactic bar, the model of superposition of inhomogeneous ellipsoids given by Pichardo et al. (2004) (see their Appendix C) has been utilized. This is a bar model which approximates the observed boxy mass distribution of the Galactic bar, and is based on a model of Freudenreich (1998) of COBE/DIRBE observations of the Galactic center. At its present position, the major axis of the bar makes

**Table 3.** Parameters of the non-axisymmetric Galactic components (Pichardo et al. 2003, 2004) used in the Galactic potential

Parameter	Value	References
<i>Spiral Arms</i>		
locus	Bisymmetric (Logthm)	1
pitch angle	$15.5^\circ$	2
external limit	12 kpc	2
scale length	2.5 kpc	Disk based
force contrast	$\sim 10 \%$	3
pattern speed	$20 \text{ km s}^{-1} \text{ kpc}^{-1}$	4
<i>Bar</i>		
major semi-axis	3.5 kpc	5
scale lengths	1.7, 0.64, 0.44 kpc	5
present major axis angle with respect to the Sun-GC line	$20^\circ$	6
mass	$1.8 \times 10^{10} M_\odot$	7
angular velocity	$60 \text{ km s}^{-1} \text{ kpc}^{-1}$	8

References. –1) Churchwell et al. (2009). 2) Drimmel (2000). 3) Patsis et al. (1991). 4) Martos et al. (2004). 5) Freudenreich (1998). 6) Gerhard (2002). 7) Calchi Novati et al. (2008); Zhao (1996); Blum (1995); Dehnen & Binney (1998); Dwek et al. (1995); Kent (1992). 8) Debattista et al. (2002); Weiner & Sellwood (1999); Fux (1999); Ibata & Gilmore (1995); Englmaier & Gerhard (1999).

an angle of approximately  $20^\circ$  with the Sun-Galactic center line. The angular velocity of the bar has been taken as  $60 \text{ km s}^{-1} \text{ kpc}^{-1}$ ; see for example Debattista et al. (2002). With this bar angular velocity and that of the spiral arms, the solar position is close to the bar 1:2 outer Lindblad resonance (OLR) and the spiral-arms’ 1:4 resonance.

The observationally motivated parameters of the non-axisymmetric Galactic components are summarized in Table 3. The corresponding parameters of the (unscaled) axisymmetric components can be found in Allen & Santillán (1991).

Figures 8 and 9 show plots of  $z_{\text{max}}$  and  $e_{\text{max}}$  versus  $r_{\text{max}}$ , respectively, for the ‘high-’ and ‘low-alpha’ halo stars, plus the thick-disk stars. ( $z_{\text{max}}$  is the extreme maximum of  $|z|$ .) In the left halves of these figures the orbital parameters are plotted from the axisymmetric Galactic model for the integration times of 5, 2, and 1 Gyr, from top to bottom, and in the right halves, the same from the non-axisymmetric model. In Figs. 10 and 11 are plotted the  $[\text{Mg}/\text{Fe}]$  and  $[\text{Na}/\text{Fe}]$  abundances as a function of the orbital parameter  $e_{\text{max}}$ , respectively, again for these same three Galactic



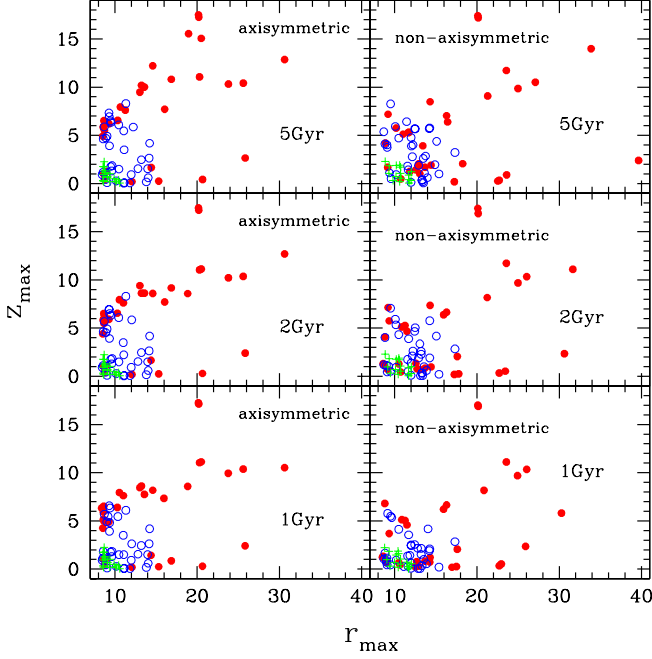


**Fig. 8.** The ‘high-alpha’ halo, ‘low-alpha’ halo, and thick-disk stars are plotted in the  $z_{\max}$  vs  $r_{\max}$  diagram for orbital integration times of 1, 2, and 5 Gyr and for both the axisymmetric and non-axisymmetric Galactic potentials. The symbols as in Fig. 5, and units of kpc for both axes.

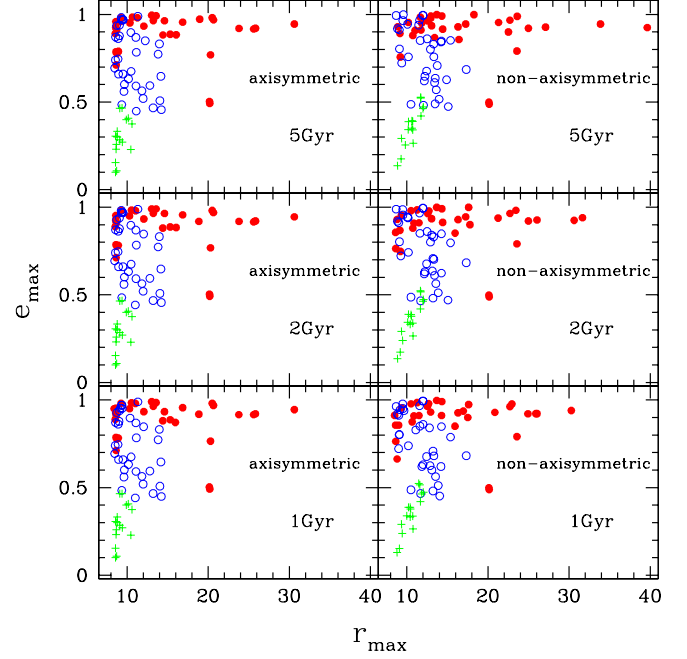


**Fig. 9.** The ‘high-alpha’ halo, ‘low-alpha’ halo, and thick-disk stars are plotted in the  $e_{\max}$  vs  $r_{\max}$  diagram for orbital integration times of 1, 2, and 5 Gyr and for both the axisymmetric and non-axisymmetric Galactic potentials. The symbols as in Fig. 5.

stellar components. Figs. 12 and 13 plot these same abundances against  $r_{\max}$ . In these last four figures the upper panels make use of orbital parameters from integrations with the axisymmetric Galactic model, and from the non-axisymmetric model in the lower panels. In all of these figures the symbols are the same as in Fig. 5.

Table 4 (online) gives the stellar ages and orbital parameters derived in Sections 3 and 4 for the halo and thick-disk stars of this paper. Columns 1 and 2 give the stellar identifications and the stellar ages with estimated errors, respectively. Columns 3–9 give the extreme minimum and maximum values, over 5 Gyr, for  $r_{\min}$ ,  $r_{\max}$ ,  $|z|_{\max}$ ,  $e_{\min}$ ,  $e_{\max}$ ,  $h_{\min}$ , and  $h_{\max}$ , respectively (where  $h$  is the angular momentum per unit mass of the star). For each star the first line gives the orbital parameters for the non-axisymmetric case and the second line for the axisymmetric. The extreme maximum values of  $r$ ,  $|z|$ , and  $e$  are those plotted in Figs. 8–13.

## 5. Discussion and conclusions

The metallicity trends of Papers I and II can be explained from existing nucleosynthesis simulations if the ‘high-alpha’ halo stars formed in regions with such a high star formation rate (SFR) that only massive stars and Type II supernovae contributed to the chemical enrichment, while the ‘low-alpha’ halo stars, on the other hand, originated from systems with a slower chemical evolution, characterized by additional enrichment from Type Ia supernovae and low-mass AGB stars. The more massive sub-units of the Galactic formation had higher densities, higher SFRs, more rapid chemical evolutions, and therefore reached higher metallicities ( $[\text{Fe}/\text{H}] \sim -0.4$  dex) before the ignition of the first

SNIa (see the  $[\alpha/\text{Fe}]$  versus  $[\text{Fe}/\text{H}]$  diagrams in Fig. 1 of McWilliam 1997, or Fig. 1 of Zolotov et al. 2010) leading to the ‘high-alpha’ halo stars, while the smaller sub-units had smaller densities, lower SFRs, slower chemical evolution, and therefore lower metallicities at the “knee” ( $[\text{Fe}/\text{H}] \lesssim -1.5$  dex, in this  $[\alpha/\text{Fe}]$  versus  $[\text{Fe}/\text{H}]$  diagram) corresponding to the ignition of the SNIa, producing ‘low-alpha’ halo stars at the higher metallicities. The question then becomes: which of the many scenarios presented in the literature to explain halo components best fits these observed abundance patterns, relative-age differences, stellar kinematics, and orbital parameters of these halo stars? For example, does the classic ELS-plus-SZ duality with a rapid collapsed, more centrally distributed halo component versus a more exterior component originating from “protogalactic fragments” accreted over several Gyr? Or, does the scattering of “*in situ*” stars from a primeval bulge or disk into the inner halo versus the accretion of stars from “subhalos” *à la* Zolotov et al. (2009, 2010) or Purcell et al. (2010)? Or, does the early accretion and merging of massive satellites but with a dichotomy of the mass distribution via the models of Robertson et al. (2005), Bullock & Johnston (2005), and Font et al. (2006a, 2006b) explain best these two halo components detected and studied here?

Our age determinations for the ‘high-’ and ‘low-alpha’ halo stars are in agreement with the conclusions of Hammer et al. (2007) and Puech et al. (2008) that the Milky Way appears to have been an “exceptionally quiet galaxy,” compared to M31 for example, having escaped any major mergers or accretions for the last  $\sim 10$  Gyr. Nearly all of the stellar ages, or average ages, in Figs. 5 and 6 and in Table 2 are greater than 9 Gyr. Whatever events produced the ‘high-alpha’ and ‘low-alpha’ halo stars occurred during the first

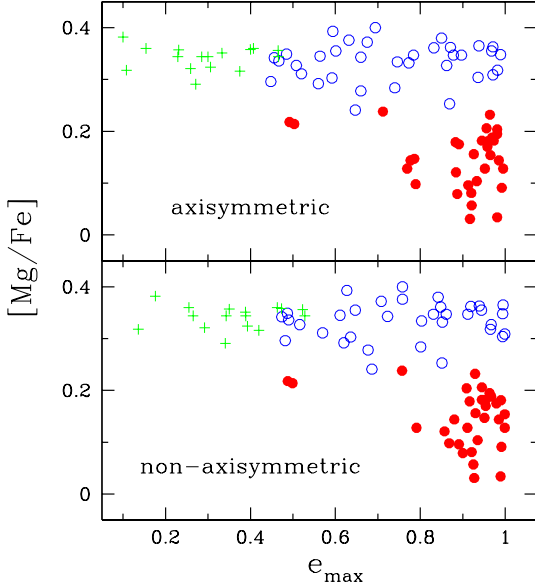


**Fig. 10.** The ‘high- $\alpha$ ’ halo, ‘low- $\alpha$ ’ halo, and thick-disk stars are plotted in the  $[\text{Mg}/\text{Fe}]$  vs  $e_{\text{max}}$  diagram for orbital integration times of 5 Gyr and for the axisymmetric Galactic potential in the upper panel, and non-axisymmetric in the lower. The symbols as in Fig. 5.

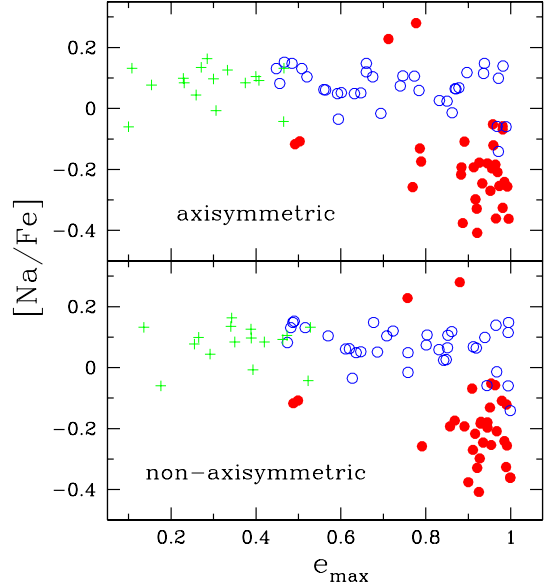


**Fig. 11.** The ‘high- $\alpha$ ’ halo, ‘low- $\alpha$ ’ halo, and thick-disk stars are plotted in the  $[\text{Na}/\text{Fe}]$  vs  $e_{\text{max}}$  diagram for orbital integration times of 5 Gyr and for the axisymmetric Galactic potential in the upper panel, and non-axisymmetric in the lower. The symbols as in Fig. 5.

few Gyr of the Galaxy’s formation. The  $\Lambda$ CDM simulations of Abadi et al. (2003a, 2003b) for disk galaxies similar to the Milky Way also show that only a very few ( $\lesssim 5$ ) major merger or accretion events occurred, and quite early, producing stellar ages today greater than nine Gyr (see their Figs. 5 and 7, respectively). Then, were these halo progenitors large enough,  $\sim 5 \times 10^{10} M_{\odot}$ , to form the ‘high- $\alpha$ ’ halo stars, as in Fig. 3 of Robertson et al. (2005), or did the gas merely combine to form a primeval bulge or disk massive enough to form the ‘high- $\alpha$ ’ halo stars with subsequent displacement into the inner halo by the same later mergers which populated the outer halo *à la* Zolotov et al. (2009, 2010) or Purcell et al. (2010)? The ‘low- $\alpha$ ’ halo stars then represent the remains of more modest accretion events which took place a couple Gyr after the stars of the ‘high- $\alpha$ ’ halo, i.e. the ‘low- $\alpha$ ’ halo stars constitute tidal debris (Navarro et al. 2011).

The ELS-plus-SZ or dual-accretion scenarios (Robertson et al. 2005; Font et al. 2006a) have difficulty explaining, or producing, high- $\alpha$  halo stars; mainly they produce one or more sequences of low- $\alpha$  halo stars. Perhaps the dual-accretion models might be salvaged using a very few, very massive accretion components which are merged and destroyed quickly to form the primeval Galaxy and its first halo component.

The orbital parameters from the integrations discussed above for the symmetric and non-symmetric Galactic potentials give some additional very important clues concerning the origins of these two halo components detected here in the Solar vicinity. For example, in Figs. 12 and 13, the abundances  $[\text{Mg}/\text{Fe}]$  and  $[\text{Na}/\text{Fe}]$ , respectively, are plotted as a function of the maximum distances from the Galactic center reached by these stars in the last 5 Gyr, with the

same symbols as in Fig. 5. And, in Figs. 10 and 11, the same abundances with the same symbols, respectively, are plotted as a function of the maximum orbital eccentricities reached by these stars in 5 Gyr. In all of the plots versus  $r_{\text{max}}$  the ‘low- $\alpha$ ’ halo stars reach much greater distances from the Galactic center than the ‘high- $\alpha$ ’ halo stars, and in all four of these plots there seems to be a correlation of decreasing  $[\text{Mg}/\text{Fe}]$  or  $[\text{Na}/\text{Fe}]$  values with increasing  $r_{\text{max}}$  for the ‘low- $\alpha$ ’ halo stars. The ‘high- $\alpha$ ’ halo stars reach a limiting  $r_{\text{max}}$  value of about 16 kpc, while the ‘low- $\alpha$ ’ halo stars go out as far as 30–40 kpc in some cases. In the plots versus the orbital eccentricities, ‘high- $\alpha$ ’ halo stars have on the average more circular orbits with a more or less uniform distribution over  $0.4 \lesssim e_{\text{max}} \lesssim 1.0$ , while the ‘low- $\alpha$ ’ ones are largely clumped at  $e_{\text{max}} \gtrsim 0.85$  with only a few exceptions. One might conclude that these results support the ideas of Zolotov et al. (2009, 2010), since the ‘high- $\alpha$ ’ halo stars populate exclusively the inner halo, ( $r_{\text{max}} \lesssim 16$ ), and exhibit a wider, uniform range in orbital eccentricities, which might be expected for stars kicked out of a primeval bulge or primeval disk by merger or accretion events.

However, most ( $\gtrsim 80\%$ ) of the *in situ* halo stars of Zolotov et al. (2009, 2010) reside within the inner  $\sim 10$  kpc of their simulated halos (see Fig. 2 of Zolotov et al. 2009, or Sect. 2.1 of Zolotov et al. 2010), contrasting with our limit here of about 16 kpc for the ‘high- $\alpha$ ’ halo stars. In addition, it is not clear whether the  $[\alpha/\text{Fe}]$  abundances of stars now residing in the Galactic Bulge are higher than those of the thick disk (Zoccali et al. 2006; Lecureur et al. 2007), or the same as the thick disk (Gonzalez et al. 2011), and in our abundance diagrams the thick-disk stars follow, or extend uniformly, the abundances of the ‘high- $\alpha$ ’ halo

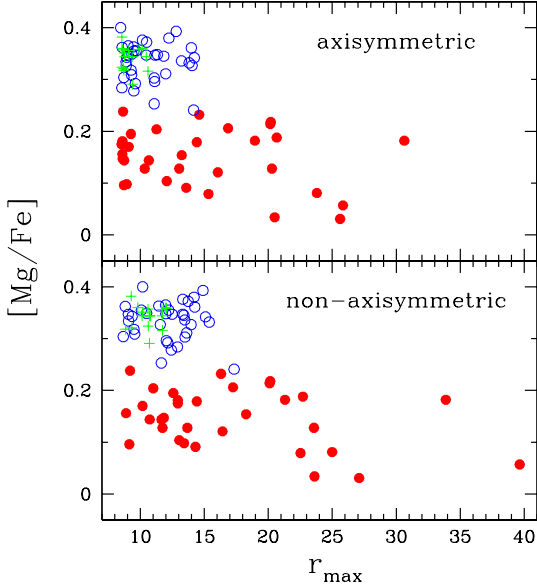


**Fig. 12.** The ‘high- $\alpha$ ’ halo, ‘low- $\alpha$ ’ halo, and thick-disk stars are plotted in the  $[\text{Mg}/\text{Fe}]$  vs  $r_{\text{max}}$  diagram for orbital integration times of 5 Gyr and for the axisymmetric Galactic potential in the upper panel, and non-axisymmetric in the lower. The symbols as in Fig. 5.

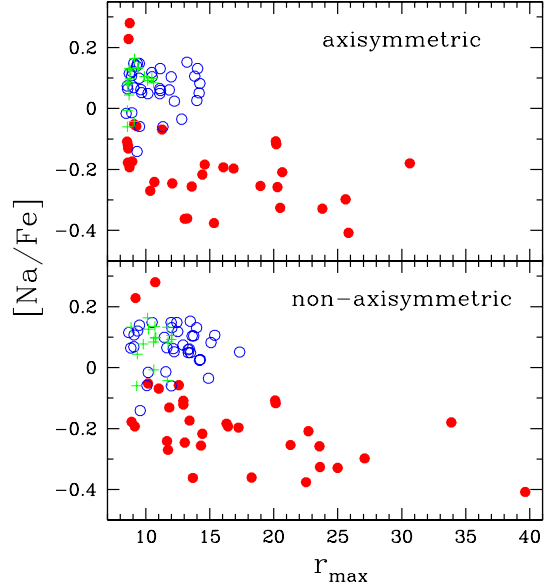


**Fig. 13.** The ‘high- $\alpha$ ’ halo, ‘low- $\alpha$ ’ halo, and thick-disk stars are plotted in the  $[\text{Na}/\text{Fe}]$  vs  $r_{\text{max}}$  diagram for orbital integration times of 5 Gyr and for the axisymmetric Galactic potential in the upper panel, and non-axisymmetric in the lower. The symbols as in Fig. 5.

stars. These facts would suggest that the displacement of *in situ* stars into the inner halo, as proposed by Zolotov et al. (2009, 2010), did not occur exclusively from the primeval bulge but also from a primeval disk, or thick disk, which extended out to nearly 16 kpc from the center of the Galaxy (Purcell et al. 2010).

The  $[\text{O}/\text{Fe}]$  versus  $[\text{Fe}/\text{H}]$  diagrams from Zolotov et al. (2010; Fig. 3) fit fairly well the  $[\alpha/\text{Fe}]$  diagrams of our Paper I (especially their models MW1 and h277), and they conclude that a galaxy which has had a long quiescent period,  $\approx 9$  Gyr, without any major mergers, should have a fairly high proportion of *in situ* halo stars ( $\approx 20\%$ – $50\%$ ) as compared to the percentage of halo stars from mergers or accretions. A galaxy with many more recent mergers might have an *in situ* halo contribution as low as 5%. Our sample includes 35 (52%) ‘high- $\alpha$ ’ halo stars and 32 (48%) of the ‘low- $\alpha$ ’ halo stars, all from the solar neighborhood, and so these percentages for our ‘high-’ and ‘low- $\alpha$ ’ halo stars agree with their large ages, 10–13 Gyr, qualitatively at least, according to these models. As mentioned above, our age determinations confirm that the Galaxy seems to have had a rather long quiescent period, without any major mergers, after the first events which formed the primeval Galaxy.

Dual-accretion  $\Lambda\text{CDM}$  models for the Galaxy (Font et al. 2006a; Robertson et al. 2005) in general do not fit as well the details of the  $[\alpha/\text{Fe}]$ , or  $[\text{Mg}/\text{Fe}]$ , versus  $[\text{Fe}/\text{H}]$  diagrams of Paper I. See for example, Fig. 9 of Font et al. (2006a), where two low- $\alpha$  sequences are produced but no high- $\alpha$  one, or Fig. 3 of Robertson et al. (2005), with a similar problem. In this latter paper, of the trichotomy of models (‘halo progenitor’, dSph, and dIrr) the first seems to come closest to producing ‘high- $\alpha$ ’ halo stars. So,

this model might be modified by increasing the mass of the progenitors and merging very quickly at the beginning of the Galaxy, combined with a dIrr model, to produce the dichotomy in the  $[\alpha/\text{Fe}]$  versus  $[\text{Fe}/\text{H}]$  diagrams of Paper I, both the ‘high-’ and ‘low- $\alpha$ ’ halo stars. (See also De Lucia & Helmi 2008 for their discussion of the ‘duality’ in their modeled stellar halo.) However, the range in age for the ‘high- $\alpha$ ’ halo stars, as seen in Table 2, is probably larger than that needed for such a scenario, especially if those in the highest metallicity range,  $-0.575 \leq [\text{Fe}/\text{H}] \leq -0.40$ , are considered.

Our relative-age sequence, with the ‘low- $\alpha$ ’ halo stars being 2–3 Gyr younger than the ‘high- $\alpha$ ’ halo stars, and the thick-disk ages lying in between, is probably congruous with any of the model-types mentioned above, ELS-plus-SZ, *in situ* plus accretion, or dual-accretion, for the formation of the Galactic halo. In the models of Zolotov et al. (2009, 2010) infalling gas forms the primeval components in which the *in situ* halo stars are formed, and then 2–3 Gyr later merger or accretion events kick these *in situ* ‘high- $\alpha$ ’ stars into the inner halo and at the same time populate the ‘low- $\alpha$ ’ component of the halo. For the dual-accretion  $\Lambda\text{CDM}$  models for the Galaxy, a very few quick and massive accretion events might produce the ‘high- $\alpha$ ’ component, and then 2–3 Gyr later a few major accretion events the ‘low- $\alpha$ ’ halo stars. The relative kinematics of these competing models for the Galactic halo are not well documented in these papers.

Recently, Font et al. (2011) have carried out new simulations of the formation of stellar halos around disk galaxies. The simulations, which include baryons in a self-consistent way, show that *in situ* star formation dominates in the inner halo ( $r < 30$  kpc), whereas most stars in the outer halo have

been accreted from satellite galaxies. An apparent gradient in  $[\text{Fe}/\text{H}]$  is predicted due to changing proportions of the *in situ* and accreted components; the metallicity drops by 0.6 - 0.9 dex from the inner to the outer halo in agreement with the analyses of SDSS data by Carollo et al. (2010) and de Jong et al. (2010). In contrast to Zolotov et al. (2009), who found that the *in situ* stars formed very early out of accreted cold gas in the inner 1 kpc region and were later displaced to the halo by mergers, Font et al. (2011) find that *in situ* halo stars formed from cooling of hot gas in a more extended inner region and were, on average, not displaced significantly from their formation site. Furthermore, they predict that the stars formed *in situ*, with ages  $\lesssim 8$  Gyr, are 3-4 Gyr younger than the accreted stars. From this it is clear that we cannot readily identify our ‘low-alpha’ and ‘high-alpha’ halo stars with the populations of accreted and *in situ* stars in the Font et al. (2011) simulations. The ‘low-alpha’ stars are about 2 Gyr younger than the ‘high-alpha’ stars (presumably formed *in situ*), and they belong to the metal-rich end of the metallicity distribution, whereas the accreted stars of Font et al. (2011) belong to the low-metallicity end. And, our ‘high-alpha’ halo stars have ages in the range 11–14 Gyrs, and orbital eccentricities, 0.4–1.0. A more detailed study is needed to see if the Font et al. (2011) simulations can produce two sequences of  $[\alpha/\text{Fe}]$  vs.  $[\text{Fe}/\text{H}]$  for metal-rich halo stars that match the age and orbital characteristics of our two halo components.

The probable correlations of the abundances  $[\text{Mg}/\text{Fe}]$  and  $[\text{Na}/\text{Fe}]$  with  $r_{\text{max}}$  for the ‘low-alpha’ halo stars are very interesting and arresting, and may provide an important clue as to their origin. (These correlations are significant at the 3–4 $\sigma$  level for  $[\text{Mg}/\text{Fe}]$  and 9–10 $\sigma$  for  $[\text{Na}/\text{Fe}]$ , excluding the two outliers, where 10% errors in  $r_{\text{max}}$  and the abundance errors in  $[\text{Mg}/\text{Fe}]$  and  $[\text{Na}/\text{Fe}]$  from Paper I have been included.) For example, these stars have probably come from progenitors falling into the Galaxy on nearly radial orbits, as shown by the large orbital eccentricities ( $e_{\text{max}} \gtrsim 0.85$ ) and low angular momenta (as seen in the Toomre diagram, Fig. 7, especially if  $V_{\text{LSR}} = 254 \text{ km s}^{-1}$ , as in the orbital integrations). The progenitors will oscillate almost radially in the Galactic potential with their maximum distances from the Galactic center slowly decreasing due to dynamic friction. At the same time these progenitors will undergo internal chemical evolution and will suffer tidal stripping each time they pass through the Galactic bulge or disk. So with time the  $r_{\text{max}}$ ’s of the progenitors will decrease, as will their total mass and their ability to retain the chemical output from the SNeIa and SNeII. At first, with higher mass, they will retain at least some of the SNeIa remnants and will contribute ‘low-alpha’ stars to the field with each tidal stripping. Later when their total mass has been reduced considerably (more than a factor of ten as has been suggested for some progenitors (Schaerer & Charbonnel 2011), the outer zones where such SNeIa remnants have been retained will be gone, and these progenitors will contribute mainly older ‘high-alpha’ stars to the field. So, according to this scenario, the dynamic time lines for the ‘low-alpha’ halo stars in Figs. 12 and 13 actually run opposite that of the chemical evolution, from right to left, rather than left to right, from large  $r_{\text{max}}$  and large mass for the progenitor, on the right, to smaller values of each on the left.

A case in point is the globular cluster  $\omega$  Cen, which is thought to have been a dwarf galaxy accreted by the Galaxy several Gyr ago. Results by Dinescu (2002) have shown metal-poor stars in the solar neighborhood with a metallicity range including that of  $\omega$  Cen, with a retrograde signature similar to  $\omega$  Cen’s orbit, and with many orbital eccentricities larger than 0.8.  $\omega$  Cen appears to have undergone considerable internal chemical evolution with at least four peaks in the  $[\text{Fe}/\text{H}]$  distribution (Johnson & Pilachowski 2010), an internal age spread of 3–8 Gyr (Hilker & Richtler 2000, 2002; Hughes & Wallerstein 2000; Hughes, Wallerstein, & van Leeuwen 2000; Rey et al. 2002; Smith et al. 2000; Smith 2002, and references therein), and, despite this significant age spread, almost no evidence of contributions from Type Ia SNe (Johnson & Pilachowski 2010; Smith et al. 2000; and Norris & Da Costa 1995); only a very few low-alpha-type stars have perhaps been found in  $\omega$  Cen (Pancino et al. 2002). It has been estimated that  $\omega$  Cen has lost more than three-fourths of its original mass (Bekki & Freeman 2003), perhaps more than 99% (Dinescu et al. 1999b, Freeman & Bland-Hawthorn 2002), and so no longer retains the SNeIa ejecta nor the zone in which low-alpha stars were produced in the past, and therefore  $\omega$  Cen no longer produces nor contributes low-alpha halo stars to the field. But with a much higher mass in the past, it may have done so with these SNeIa ejecta accumulating in an outer shell of the progenitor. In Paper II a comparison between the ‘low-alpha’ halo stars and  $\omega$  Cen was made due to a similarity in the (U,V,W) Galactic velocities, and conclusions drawn similar to those above due to the lack now of any significant number of stars showing enrichment by SNeIa ejecta. The above scenario explains how  $\omega$  Cen may have contributed significantly to the ‘low-alpha’ halo stars, and yet nowadays have so very few of these.

Our Galactic mass model, with the bar only, and using the measured absolute proper motions for  $\omega$  Cen from Dinescu et al. (1999a, 1999b), has been used to integrate its orbit for 5 Gyr, producing an apogalactic distance of about 7.5 kpc, a perigalactic distance of about 0.5 kpc,  $z_{\text{max}} \approx 3.7$  kpc, and  $e_{\text{max}} \approx 0.87$ . This eccentricity agrees with those of the ‘low-alpha’ halo stars in Fig. 9, but these  $r_{\text{max}}$  and  $z_{\text{max}}$  values fall far short as seen in Fig. 8 with values of  $r_{\text{max}}$  out to 30–40 kpc and  $z_{\text{max}}$  values generally above 5 kpc for the ‘low-alpha’ halo stars. Dinescu et al. (1999b) also used these absolute proper motions to integrate Galactic orbits for  $\omega$  Cen with two different Galactic mass models giving an apogalactic distance of about 6.2 kpc and a perigalactic distance of about 1.2 kpc, with  $z_{\text{max}} \approx 1.0$  kpc and  $e \approx 0.67$ . These values agree even less with the typical orbital parameters of the ‘low-alpha’ halo stars.

Simulations by Zhao (2002) would suggest that  $\omega$  Cen would have had to be launched near the edge of the Galactic disk with  $R \approx 15$  kpc,  $|Z| \approx 1$  kpc, and a retrograde velocity to obtain its observed mass and apo- and perigalactic distances in about a Hubble time; these simulations take into account dynamical friction and tidal stripping, unlike the orbital integrations mentioned above. Again these initial conditions and orbital characteristics are not in good agreement with our orbital parameters for many of the ‘low-alpha’ halo stars. The simulations of Bekki & Freeman (2003) for the orbit and tidal stripping of  $\omega$  Cen might yield accreted stars out to about  $R = 26$  kpc in 2.6 Gyr, and produce approximately the current apogalactic distance of  $\omega$  Cen, 8 kpc, which compares well with the 7.5 kpc value

obtained with our Galactic mass model. That simulation which approximately fits the current orbital parameters of  $\omega$  Cen, and at the same time spans well our ‘low-alpha’ halo stars, has been obtained by Tsuchiya et al. (2003, 2004) by providing  $\omega$  Cen with  $M_{\text{tot}} = 8 \times 10^9 M_{\odot}$  at the beginning of the integrations, a Hernquist density profile (their model H4), a launching distance of  $R = 58$  kpc, i.e. 50 kpc from the rotation axis and 30 kpc above the Galactic plane, with a retrograde velocity of  $-20 \text{ km s}^{-1}$  in the direction of Galactic rotation, and zero velocities in the other two directions; they obtain current apogalactic and perigalactic distances of about 6 and 1 kpc, and a remaining mass for  $\omega$  Cen of approximately  $10^7 M_{\odot}$  after about 3 Gyr. Their method improves on simplifications made by Zhao (2002); for example, they have also included dynamical friction from the Galactic bulge and disk. This model could produce stripped stars like the ‘low-alpha’ halo stars, with  $r_{\text{max}}$ ’s to 40 kpc,  $z_{\text{max}}$ ’s greater than 5 kpc, and very eccentric orbits.

So, if  $\omega$  Cen has made a significant contribution to our ‘low-alpha’ halo stars, this would imply that it has probably suffered very significant dynamical friction and tidal stripping. Some of the above models estimate that it has lost more than 99% of its original mass, for example, from  $8 \times 10^9 M_{\odot}$  to about  $1 \times 10^7 M_{\odot}$  in the models of Tsuchiya et al. (2003, 2004). This would help explain why and how  $\omega$  Cen now has almost no stars with evidence of contributions from Type Ia SNe (Johnson & Pilachowski 2010; Smith et al. 2000; and Norris & Da Costa 1995), but may have contributed in the past a significant portion of the ‘low-alpha’ halo stars now seen in the solar neighborhood. The type Ia SNe remnants were deposited mostly in the outer regions of its progenitor, and these have by now been stripped away. In analogy, significant differences between the abundances of the Sagittarius dwarf galaxy and its stream have been detected by Chou et al. (2007, 2010).

Due to the large ages with a moderately small dispersion of the ‘low-alpha’ halo stars, it is improbable that the Sagittarius dwarf galaxy has contributed to their presence in the solar neighborhood; this dwarf galaxy is most likely on one of its first passes near the Milky Way (Ibata et al. 1995) and contains a mixture of stars with ages from about 6 Gyr to more than 9 Gyr (Bellazzini et al. 2006). In agreement, both local radial velocity surveys and calculations of this dwarf galaxy’s orbit have concluded that it has not passed through the solar neighborhood (for example, Seabroke et al. 2008; Newberg et al. 2007).

Very recent results by Tan & Zhao (2011) supplement and support the results of our Papers I, II, and III. They have obtained beryllium abundances, on a uniform scale, for 43 of our halo and thick-disk stars, including 14 thick-disk stars, 13 ‘low-alpha’, and 16 ‘high-alpha’ halo stars. They find very clear evidence for separate sequences between the ‘low-alpha’ and ‘high-alpha’ (halo plus thick-disk) stars in the  $A(\text{Be})$  versus  $[\text{Fe}/\text{H}]$ , and  $A(\text{Be})$  versus  $[\alpha/\text{H}]$  diagrams, with the ‘high-alpha’ stars having larger  $A(\text{Be})$  values for a given value of  $[\text{Fe}/\text{H}]$ , or  $[\alpha/\text{H}]$ . Since Be is formed by cosmic-ray reactions, these results would suggest that these two stellar components have formed in regions with different strengths of the cosmic-ray field, such as a low-mass dwarf galaxy versus a high-mass primeval bulge or disk.

From this discussion of our results, we draw the following conclusions about stars belonging to the metal-rich end ( $[\text{Fe}/\text{H}] > -1.6$ ) of the halo metallicity distribution.

1. The ages of both the ‘high-’ and ‘low-alpha’ halo stars are large, 10-13 Gyr, supporting the idea, presented in many works in the literature, that the Galaxy has had a rather quiescent history for the last 9 Gyr, or more, without any major mergers. Also, our ages from the  $Y^2$  isochrones, interpolated to the exact  $[\text{Fe}/\text{H}]$  and  $[\alpha/\text{Fe}]$  values of the spectroscopic analyses, indicate that the ‘high-alpha’ halo stars are 2-3 Gyr older than the ‘low-alpha’, with the possibility that the thick-disk stars have ages intermediate between these two halo components.
2. The *in situ*-accretion models of Zolotov et al. (2009, 2010) can explain more naturally both the ‘high-’ and ‘low-alpha’ halo stars. Infalling gas forms a primeval bulge or disk which in turn produce *in situ* stars that are then scattered into the inner halo by the same accretion events which bring into the Galaxy the ‘low-alpha’ halo stars. Both *in situ* and accreted stellar products end up in the Galactic halo, with greatly differing but overlapping distributions, as seen in the orbital parameters of our two halo components, and these are found in our halo sample with nearly equal numbers in agreement with the recent quiescent history of the Milky Way.
3. The distribution of orbital eccentricities is quite different between the ‘high-’ and ‘low-alpha’ halo stars; see Figs. 9–11. This supports the idea of different formation scenarios for these two components, such as scattered *in situ* halo stars versus accreted halo stars, respectively, with the thick-disk being an extension of the ‘high-alpha’ halo, or vice versa.
4. The distributions of  $r_{\text{max}}$  and  $z_{\text{max}}$  are also significantly different between the ‘high-’ and ‘low-alpha’ halo stars; see Fig. 8. The ‘low-alpha’ ones reach out to  $r_{\text{max}} \approx 30$ –40 kpc, while the ‘high-alpha’ only to  $r_{\text{max}} \approx 16$  kpc, and for  $z_{\text{max}}$ , the ‘low-alpha’ halo stars reach much higher levels,  $\approx 18$  kpc, than the ‘high-alpha’ ones,  $\approx 6$ –8 kpc; these latter values are in line with the heights produced by scattering from a primeval disk in the simulations of Purcell et al. (2010). However, the *in situ* halo stars of the models are in general scattered from the bulge into the inner halo with  $r_{\text{max}}$ ’s less than 10 kpc; more than 80% have  $r_{\text{max}} < 10$  kpc, suggesting that more energetic scattering from the primeval bulge is required in the models of Zolotov et al. (2009, 2010).
5. Significant correlations between the abundances  $[\text{Mg}/\text{Fe}]$  or  $[\text{Na}/\text{Fe}]$  and the orbital parameter  $r_{\text{max}}$  are seen in Figs. 12 and 13 for the ‘low-alpha’ halo stars. We suggest that these correlations have to do with the combined effects of tidal stripping and dynamical friction on the progenitors of the ‘low-alpha’ halo stars, combined with internal chemical evolution and radial and temporal variations in the retention of SNeIa remnants. Such a scenario fits well the suggestion that  $\omega$  Cen has contributed in a significant way to the ‘low-alpha’ halo stars.
6. The models of Tsuchiya et al. (2003, 2004) give a reasonable fit to the current mass and orbital characteristics of  $\omega$  Cen, while at the same time providing a feasible explanation for the large values of  $r_{\text{max}}$ ,  $z_{\text{max}}$ , and  $e_{\text{max}}$  of the ‘low-alpha’ halo stars as seen in Figs. 8 and 9. Their orbital integrations were begun with the progenitor 58 kpc from the Galactic center, and with a retrograde rotational velocity of  $-20 \text{ km s}^{-1}$ . Such initial conditions are probably representative of other dwarf

galaxies which may have contributed to the ‘low- $\alpha$ ’ halo stars.

As epilogue, it seems that evidence in the Milky Way is ubiquitous, and probably in many other galaxies as well, for some sort of dominating, quick event at the very beginning of galaxy formation, such as a rapid monolithic collapse of a protogalactic cloud à la ELS, which would have produced the high- $\alpha$  halo stars. This evidence is seen in the main sequence turnoffs as studied in the SDSS data by Jofré & Weiss (2011) and in the  $(b-y)_{0,TO}$  versus  $[Fe/H]$  diagram for high-velocity and metal-poor halo stars of Schuster et al. (2006). This evidence is also clear in the old-group globular clusters of Marín-Franch et al. (2009) with a mean age of about 12.8 Gyr and an intrinsic dispersion of only about 0.4 Gyr, and in the older population of numerous early-type galaxies encountered by Rakos et al. (2008) with ages of 11–12 Gyr. Such a quick, significant, and early event would also be needed to produce the high- $\alpha$  halo stars of this paper with metallicities as high as  $[Fe/H] \approx -0.4$  before the ignition of SNeIa, and ages as large as 11–12 Gyr. This goes whether or not they were collapsed, merged, or accreted directly into the Galactic halo, or scattered there. However, such a quick and early event is not compatible with hierarchical galaxy-formation schemes which require the gradual merging of smaller units to form large galaxies.

Also, the low- $\alpha$  halo stars pose a quandary, together with the results of Marín-Franch et al. (2009) for their young-group, probably-accreted, globular clusters. In Paper II of this series it has been shown that the dispersions of the low- $\alpha$  sequences are larger than the expected observational spectroscopic errors with values of 0.04–0.06 dex for the  $\alpha$  elements, and dispersions as large as 0.11–0.15 dex for  $[Na/Fe]$  and  $[Cu/Fe]$ . It was suggested that this is due to the accretion of an ensemble of dwarf galaxies with slightly different star-formation histories. But the question arises: why is this scatter not much larger? Figure 4 of Zolotov et al. (2010) would suggest a much wider low- $\alpha$  sequence, perhaps 0.3 dex or more in  $[\alpha/Fe]$  at a given  $[Fe/H]$ , for any significant and reasonable range for the masses of these accreted dwarf galaxies. And, the  $[\alpha/Fe]$  versus  $[Fe/H]$  diagrams of Tolstoy et al. (2009; Fig. 11) for high-resolution spectroscopy of giant stars in four dwarf spheroidal galaxies would suggest a range as large as 0.3 dex (e.g. between Sculptor, Fornax, and Sagittarius). In this same context, Marín-Franch et al. (2009) question why all of their young-group accreted globular cluster follow the same age-metallicity sequence (i.e. similar to an  $[\alpha/Fe]$  versus  $[Fe/H]$  sequence) if they have been accreted from different dwarf galaxies, such as Sagittarius, Monoceros, and Canis Major? Does this indicate that all previous dwarf galaxies shared very similar star-formation and chemical-enrichment histories, which as Marín-Franch et al. (2009) point out seems very “unlikely”? Why should all of these dwarf galaxies (or their globular clusters) have had similar initial masses?

*Acknowledgements.* This publication made use of the SIMBAD database operated at CDS, Strasbourg, France, and of data products from the Two Micron All Sky Survey, which is a joint project of the University of Massachusetts and the Infrared Processing and Analysis Center/California Institute of Technology, funded by NASA and the National Science Foundation. This research has made use of NASA’s Astrophysics Data System. The staff at the Nordic Optical Telescope is thanked for competent and friendly assistance in obtaining spectra for this project, and the referee, Timothy Beers, for constructive and useful suggestions.

## References

- Abadi, M. G., Navarro, J. F., Steinmetz, M., & Eke, V. R. 2003a, *ApJ*, 591, 499
- Abadi, M. G., Navarro, J. F., Steinmetz, M., & Eke, V. R. 2003b, *ApJ*, 597, 21
- Allen, C., & Santillán, A. 1991, *Rev. Mexicana Astron. Astrofis.*, 22, 255
- Allen, C., Schuster, W. J. & Poveda, A. 1991, *A&A*, 244, 280
- Allen, C., Moreno, E., & Pichardo, B. 2006, *ApJ*, 652, 1150
- Allen, C., Moreno, E., & Pichardo, B. 2008, *ApJ*, 674, 237
- Alonso, A., Arribas, S., & Martínez-Roger, C. 1995, *A&A*, 297, 197
- Alves-Brito, A., Meléndez, J., Asplund, M., Ramírez, I., & Yong, D. 2010, *A&A*, 513, A35
- Beers, T. C., Carollo, D., Ivezić, Ž., et al. 2011, preprint (arXiv:1104.2513)
- Bekki, K., & Freeman, K. C. 2003, *MNRAS*, 346, L11
- Bellazzini, M., Correnti, M., Ferraro, F. R., Monaco, L., & Montegriffo, P. 2006, *A&A*, 446, L1
- Blum, R. D. 1995, *ApJ*, 444, L89
- Bohlin, R. C. 2007, in *The Future of Photometric, Spectrophotometric, and Polarimetric Standardization*, ed. C. Sterken, ASP Conf. Ser., 364, (Astronomical Society of the Pacific, San Francisco), 315
- Bullock, J. S., & Johnston, K. V. 2005, *ApJ*, 635, 931
- Buta, R., Laurikainen, E., & Salo, H. 2004, *AJ*, 127, 279
- Buta, R., Vasylyev, S., Salo, H., & Laurikainen, E. 2005, *AJ*, 130, 506
- Calchi Novati, S., de Luca, F., Jetzer, Ph., Mancini, L., & Scarpetta, G. 2008, *A&A*, 480, 723
- Carollo, D., Beers, T. C., Lee, Y. S., et al. 2007, *Nature*, 450, 1020
- Carollo, D., Beers, T. C., Chiba, M., et al. 2010, *ApJ*, 712, 692
- Casagrande, L., Ramírez, I., Meléndez, J., Bessell, M., & Asplund, M. 2010, *A&A*, 512, A54
- Casagrande, L., Schönrich, R., Asplund, M., et al. 2011, *A&A*, 530, A138
- Chou, M.-Y., Majewski, S. R., Cunha, K., et al. 2007, *ApJ*, 670, 346
- Chou, M.-Y., Cunha, K., Majewski, S. R., et al. 2010, *ApJ*, 708, 1290
- Churchwell, E., Babler, B. L., Meade, M. R., et al. 2009, *PASP*, 121, 213
- Combes, F., & Sanders, R. H. 1981, *A&A*, 96, 164
- Debatista, V. P., Gerhard, O., & Sevenster, M. N. 2002, *MNRAS*, 334, 355
- Dehnen, W., & Binney, J. 1998, *MNRAS*, 294, 429
- de Jong, J. T. A., Yanny, B., Rix, H.-W., et al. 2010, *ApJ*, 714, 663
- De Lucia, G. & Helmi, A. 2008, *MNRAS*, 391, 14
- Demarque, P., Woo, J.-H., Kim, Y.-C., & Yi, S. K. 2004, *ApJS*, 155, 667
- Dinescu, D. I. 2002, in  *$\omega$  Centauri: A Unique Window into Astrophysics*, ed. F. van Leeuwen, J. D. Hughes, & G. Piotto, ASP Conf. Ser., 265, (Astronomical Society of the Pacific, San Francisco), 365
- Dinescu, D. I., van Altena, W. F., Girard, T. M., & López, C. E. 1999a, *AJ*, 117, 277
- Dinescu, D. I., Girard, T. M., & van Altena, W. F. 1999b, *AJ*, 117, 1792
- Dotter, A., Sarajedini, A., Anderson, J., et al. 2010, *ApJ*, 708, 698
- Drimmel, R. 2000, *A&A*, 358, L13
- Drimmel, R., & Spergel, D. N. 2001, *ApJ*, 556, 181
- Ducati, J.R., Penteado, E.M., & Turcati, R. 2011, *A&A*, 525, A26
- Dwek, E., Arendt, R. G., Hauser, M. G., et al. 1995, *ApJ*, 445, 716
- Eggen, O. J., Lynden-Bell, D., & Sandage, A. R. 1962, *ApJ*, 136, 748
- Englmaier, P., & Gerhard, O. 1999, *MNRAS*, 304, 512
- ESA 1997, *The Hipparcos and Tycho Catalogues*, ESA SP-1200
- Font, A. S., Johnston, K. V., Bullock, J. S., & Robertson, B. E. 2006a, *ApJ*, 638, 585
- Font, A. S., Johnston, K. V., Bullock, J. S., & Robertson, B. E. 2006b, *ApJ*, 646, 886
- Font, A. S., McCarthy, I. G., Crain, R. A., et al. 2011, *MNRAS*, 416, 2802
- Freeman, K. & Bland-Hawthorn, J. 2002, *ARA&A*, 40, 487
- Freudenreich, H. T. 1998, *ApJ*, 492, 495
- Fux, R. 1999, *A&A*, 345, 787
- Gerhard, O. 2002, in *The Dynamics, Structure & History of Galaxies: A Workshop in Honour of Professor Ken Freeman*, ed. G. S. Da Costa & H. Jerjen, ASP Conf. Ser., 273, (Astronomical Society of the Pacific, San Francisco), 73
- Gilmore, G., Wyse, R. F. G., & Kuijken, K. 1989, *ARA&A*, 27, 555



- Gonzalez, O. A., Rejkuba, M., Zoccali, M., et al. 2011, *A&A*, 530, A54
- Gustafsson, B., & Mizuno-Wiedner, M. 2001, in *Astrophysical Ages and Time Scales*, ed. T. von Hippel, C. Simpson, & N. Manset, ASP Conf. Ser., 245, (Astronomical Society of the Pacific, San Francisco), 271
- Gustafsson, B., Edvardsson, B., Eriksson, K. et al. 2008, *A&A*, 486, 951
- Hammer, F., Puech, M., Chemin, L., Flores, H., & Lehnert, M. D. 2007, *ApJ*, 662, 322
- Helmi, A. 2008, *A&A Rev.*, 15, 145
- Hilker, M., & Richtler, T. 2000, *A&A*, 362, 895
- Hilker, M., & Richtler, T. 2002, in  $\omega$  Centauri: A Unique Window into Astrophysics, ed. F. van Leeuwen, J. D. Hughes, & G. Piotto, ASP Conf. Ser., 265, (Astronomical Society of the Pacific, San Francisco), 59
- Høg, E., Fabricius, C., Makarov, V. V. et al. 2000, *A&A*, 355, L27
- Hughes, J., & Wallerstein, G. 2000, *AJ*, 119, 1225
- Hughes, J., Wallerstein, G., & van Leeuwen, F. 2002, in  $\omega$  Centauri: A Unique Window into Astrophysics, ed. F. van Leeuwen, J. D. Hughes, & G. Piotto, ASP Conf. Ser., 265, (Astronomical Society of the Pacific, San Francisco), 73
- Ibata, R. A., & Gilmore, G. F. 1995, *MNRAS*, 275, 605
- Jarosik, N., Bennett, C. L., Dunkley, J., et al. 2011, *ApJS*, 192, 14
- Johnson, C. I., & Pilachowski, C. A. 2010, *ApJ*, 722, 1373
- Jofré, P. & Weiss, A. 2011, *A&A*, 533, A59
- Kent, S. M. 1992, *ApJ*, 387, 181
- Kim, Y.-C., Demarque, P., Yi, S. K., & Alexander, D. R. 2002, *ApJS*, 143, 499
- Kurucz, R. L., Furenlid, I., Brault, J., & Testerman, L. 1984, *Solar Flux Atlas from 296 to 1300 nm*, (National Solar Observatory, Sunspot, New Mexico)
- Larson, D., Dunkley, J., Hinshaw, G. et al. 2011, *ApJS*, 192, 16
- Latham, D. W., Stefanik, R. P., Torres, G., et al. 2002, *AJ*, 124, 1144
- Lebreton, Y. 2000, *ARA&A*, 38, 35
- Lecureur, A., Hill, V., Zoccali, M., et al. 2007, *A&A*, 465, 799
- Marín-Franch, A., Aparicio, A., Piotto, G., et al. 2009, *ApJ*, 694, 1498
- Márquez, A., & Schuster, W. J. 1994, *A&AS*, 108, 341
- Martos, M., Hernández, X., Yáñez, M., Moreno, E., & Pichardo, B. 2004, *MNRAS*, 350, L47
- McWilliam, A. 1997, *ARA&A*, 35, 503
- Morrison, H. L., Helmi, A., Sun, J. et al. 2009, *ApJ*, 694, 130
- Navarro, J. F., Abadi, M. G., Venn, K. A., Freeman, K. C., & Anguiano, B. 2011, *MNRAS*, 412, 1203
- Newberg, H. J., Yanny, B., Cole, N., et al. 2007, *ApJ*, 668, 221
- Nissen, P. E. 1994, *Rev. Mexicana Astron. Astrofis.*, 29, 129
- Nissen, P. E., & Schuster, W. J. 1991, *A&A*, 251, 457
- Nissen, P. E., & Schuster, W. J. 2010, *A&A*, 511, L10 (paper I)
- Nissen, P. E., & Schuster, W. J. 2011, *A&A*, 530, A15 (paper II)
- Norris, J. E., & Da Costa, G., S. 1995, *ApJ*, 447, 680
- Pancino, E., Pasquini, L., Hill, V., Ferraro, F. R., & Bellazzini, M. 2002, *ApJ*, 568, L101
- Patsis, P. A., Contopoulos, G., & Grosbol, P. 1991, *A&A*, 243, 373
- Pichardo, B., Martos, M., Moreno, E., & Espresate, J. 2003, *ApJ*, 582, 230
- Pichardo, B., Martos, M., & Moreno, E. 2004, *ApJ*, 609, 144
- Press, W. H., Teukolsky, S. A., Vetterling, W. T., & Flannery, B. P. 1992, *Numerical Recipes in FORTRAN 77: The Art of Scientific Computing*, 2nd ed., (Cambridge Univ. Press, Cambridge)
- Puech, M., Hammer, F., Chemin, L., Flores, H., & Lehnert, M. 2008, in *Formation and Evolution of Galaxy Disks*, ed. J. G. Funes, & E. M. Corsini, ASP Conf. Ser., 396, (Astronomical Society of the Pacific, San Francisco), 287
- Purcell, C.W., Bullock, J.S., & Kazantzidis, S. 2010, *MNRAS*, 404, 1711
- Rakos, K., Schombert, J., & Odell, A. 2008, *ApJ*, 677, 1019
- Ramírez, I., & Meléndez, J. 2005, *ApJ*, 626, 465
- Reid, M. J., Menten, K. M., Zheng, X. W., et al. 2009, *ApJ*, 700, 137
- Rey, S.-C., Joo, J.-M., Sohn, Y.-J., Ree, C. H., & Lee, Y.-W. 2002, in  $\omega$  Centauri: A Unique Window into Astrophysics, ed. F. van Leeuwen, J. D. Hughes, & G. Piotto, ASP Conf. Ser., 265, (Astronomical Society of the Pacific, San Francisco), 177
- Robertson, B., Bullock, J. S., Font, A. S., Johnston, K. V., & Hernquist, L. 2005, *ApJ*, 632, 872
- Sanders, R. H., & Tubbs, A. D. 1980, *ApJ*, 235, 803
- Schaerer, D., & Charbonnel, C. 2011, *MNRAS*, 413, 2297
- Schönrich, R., Asplund, M., & Casagrande, L. 2011, *MNRAS*, 415, 3807
- Schuster, W. J., & Allen, C. 1997, *A&A*, 319, 796
- Schuster, W. J., & Nissen, P. E. 1989, *A&A*, 221, 65
- Schuster, W. J., Beers, T. C., Michel, R., Nissen, P. E., & García, G. 2004, *A&A*, 422, 527
- Schuster, W. J., Moitinho, A., Márquez, A., Parrao, L., & Covarrubias, E. 2006, *A&A*, 445, 939
- Seabroke, G. M., Gilmore, G., Siebert, A., et al. 2008, *MNRAS*, 384, 11
- Searle, L. & Zinn, R. 1978, *ApJ*, 225, 357
- Skrutskie, M. F., Cutri, R. M., Stiening, R., et al. 2006, *AJ*, 131, 1163
- Smith, V. V. 2002, in  $\omega$  Centauri: A Unique Window into Astrophysics, ed. F. van Leeuwen, J. D. Hughes, & G. Piotto, ASP Conf. Ser., 265, (Astronomical Society of the Pacific, San Francisco), 109
- Smith, V. V., Suntzeff, N. B., Cunha, K., et al. 2000, *AJ*, 119, 1239
- Takeda, Y., & Takada-Hidai, M. 2011, *PASJ*, 63, S537
- Tan, K., & Zhao, G. 2011, *ApJ*, 738, L33
- Tolstoy, E., Hill, V., & Tosi, M. 2009, *ARA&A*, 47, 371
- Tsuchiya, T., Dinescu, D. I., & Korchagin, V. I. 2003, *ApJ*, 589, L29
- Tsuchiya, T., Korchagin, V. I., & Dinescu, D. I. 2004, *MNRAS*, 350, 1141
- VandenBerg, D. A. 1983, *ApJS*, 51, 29
- VandenBerg, D. A., Swenson, F. J., Rogers, F. J., Iglesias, C. A., & Alexander, D. R. 2000, *ApJ*, 532, 430
- van Leeuwen, F. 2007, *Hipparcos, the New Reduction of the Raw Data*, *Astrophys. Space Sci. Library*, vol. 350, (Springer, Dordrecht)
- Weiner, B. J., & Sellwood, J. A. 1999, *ApJ*, 524, 112
- Yi, S., Demarque, P., Kim, Y.-C., et al. 2001, *ApJS*, 136, 417
- Yi, S. K., Kim, Y.-C., & Demarque, P. 2003, *ApJS*, 144, 259
- Zhao, H. 1996, *MNRAS*, 278, 488
- Zhao, H. S. 2002, in  $\omega$  Centauri: A Unique Window into Astrophysics, ed. F. van Leeuwen, J. D. Hughes, & G. Piotto, ASP Conf. Ser., 265, (Astronomical Society of the Pacific, San Francisco), 391
- Zinn, R. 1993, in *The Globular Clusters-Galaxy Connection*, ed. G. H. Smith, & J. P. Brodie, ASP Conf. Ser. 48, (Astronomical Society of the Pacific, San Francisco), 38
- Zoccali, M., Lecureur, A., Barbuy, B., et al. 2006, *A&A*, 457, L1
- Zolotov, A., Willman, B., Brooks, A. M., et al. 2009, *ApJ*, 702, 1058
- Zolotov, A., Willman, B., Brooks, A. M., et al. 2010, *ApJ*, 721, 738

**Table 1.** Spectroscopic and photometric values of  $T_{\text{eff}}$  and  $\log g$  for stars without detectable interstellar NaD lines.

ID	$T_{\text{eff}}(\text{spec})$ [K]	$\log g(\text{spec})$ [cgs]	[Fe/H]	$[\alpha/\text{Fe}]$	$T_{\text{eff}}(b-y)$ [K]	$T_{\text{eff}}(V-K)$ [K]	$\log g(\text{HIP})$ [cgs]	Comment
BD-21 3420	5808	4.26	-1.13	0.31	5855	5884	$4.09 \pm 0.18$	
CD-33 3337	5979	3.86	-1.36	0.30	6005	5924	$4.08 \pm 0.08$	
CD-45 3283	5597	4.55	-0.91	0.12	5646	5616	$4.71 \pm 0.13$	
CD-57 1633	5873	4.28	-0.90	0.07	5964	5874	$4.26 \pm 0.08$	
G13-38	5263	4.54	-0.88	0.32	5241	5279	$4.45 \pm 0.12$	
G18-28	5372	4.41	-0.83	0.31	5376	5320	$4.58 \pm 0.08$	SB1 (1)
G46-31	5901	4.23	-0.83	0.15	5918	5811	$4.15 \pm 0.40$	SB1 (1)
G56-30	5830	4.26	-0.89	0.11	5871	5824		
G82-05	5277	4.45	-0.75	0.09	5312	5293	$4.73 \pm 0.14$	
G85-13	5628	4.38	-0.59	0.28	5631	5681	$4.31 \pm 0.20$	
G94-49	5373	4.50	-0.80	0.31	5346	5363		
G99-21	5487	4.39	-0.67	0.29	5528	5536	$4.31 \pm 0.27$	
G119-64	6181	4.18	-1.48	0.28	6129	6165	$4.07 \pm 0.15$	
G121-12	5928	4.23	-0.93	0.10	5913	5919	$4.17 \pm 0.24$	
G159-50	5624	4.37	-0.93	0.31	5622	5660	$4.29 \pm 0.08$	
G172-61	5225	4.47	-1.00	0.19	5282	5242		SB1 (1)
G176-53	5523	4.48	-1.34	0.18	5522	5595	$4.36 \pm 0.10$	
G180-24	6004	4.21	-1.39	0.33	5958	5986	$4.18 \pm 0.11$	
G232-18	5559	4.48	-0.93	0.32	5505	5546		
HD3567	6051	4.02	-1.16	0.21	6027	6014	$4.12 \pm 0.10$	
HD17820	5773	4.22	-0.67	0.29	5736	5787	$4.20 \pm 0.06$	
HD22879	5759	4.25	-0.85	0.31	5763	5754	$4.25 \pm 0.03$	
HD25704	5868	4.26	-0.85	0.24	5752	5659	$4.20 \pm 0.04$	$\Delta H_p = 3.49, \rho = 1''.10$ (2)
HD51754	5767	4.29	-0.58	0.26	5769	5814	$4.24 \pm 0.08$	
HD59392	6012	3.91	-1.60	0.32	5992	5976	$3.99 \pm 0.15$	
HD76932	5877	4.13	-0.87	0.29	5883	5871	$4.13 \pm 0.03$	
HD97320	6008	4.19	-1.17	0.28	5979	5992	$4.22 \pm 0.04$	
HD106516	6196	4.42	-0.68	0.29	6202	6169	$4.36 \pm 0.03$	SB1 (3)
HD114762A	5856	4.21	-0.70	0.24	5815	5748	$4.19 \pm 0.04$	
HD120559	5412	4.50	-0.89	0.30	5361	5352	$4.56 \pm 0.04$	
HD121004	5669	4.37	-0.70	0.32	5596	5601	$4.36 \pm 0.07$	
HD126681	5507	4.45	-1.17	0.35	5506	5497	$4.61 \pm 0.06$	
HD148816	5823	4.13	-0.73	0.27	5809	5803	$4.10 \pm 0.04$	
HD159482	5737	4.31	-0.73	0.30	5687	5614	$4.36 \pm 0.06$	$\Delta H_p = 1.47, \rho = 0''.27$ (2)
HD175179	5713	4.33	-0.65	0.29	5687	5719	$4.31 \pm 0.08$	
HD177095	5349	4.39	-0.74	0.31	5321	5375	$4.45 \pm 0.08$	
HD189558	5617	3.80	-1.12	0.33	5612	5652	$3.82 \pm 0.05$	
HD193901	5656	4.36	-1.09	0.16	5636	5743	$4.47 \pm 0.05$	
HD194598	5942	4.33	-1.09	0.18	5936	6000	$4.22 \pm 0.05$	
HD199289	5810	4.28	-1.04	0.30	5754	5849	$4.23 \pm 0.05$	
HD205650	5698	4.32	-1.17	0.30	5691	5808	$4.44 \pm 0.06$	
HD219617	5862	4.28	-1.45	0.28	5887	5967	$4.26 \pm 0.11$	$\Delta H_p = 0.22, \rho = 0''.82$ (2)
HD222766	5334	4.27	-0.67	0.30	5380	5380	$4.14 \pm 0.19$	
HD230409	5318	4.54	-0.85	0.27	5258	5336	$4.49 \pm 0.11$	
HD233511	6006	4.23	-1.55	0.34	5932	5985	$4.28 \pm 0.14$	
HD237822	5603	4.33	-0.45	0.29	5621	5611	$4.49 \pm 0.13$	
HD241253	5831	4.31	-1.10	0.29	5834	5897	$4.15 \pm 0.18$	
HD250792A	5489	4.47	-1.01	0.24	5511	5363	$4.37 \pm 0.11$	$\Delta H_p = 2.11, \rho = 0''.22$ (2)

References: (1) Latham et al. (2002). (2) ESA (1997). (3) Ducati et al. (2011).



**Table 4.** Stellar ages, and orbital parameters with the non-axisymmetric and axisymmetric potentials (5 Gyr integrations).

Star	Age $\pm\sigma$ Age (Gyr)	$r_{\min}$ (kpc)	$r_{\max}$ (kpc)	$ z _{\max}$ (kpc)	$e_{\min}$	$e_{\max}$	$h_{\min}$ (/10 km s $^{-1}$ kpc)	$h_{\max}$ (/10 km s $^{-1}$ kpc)
BD-21 3420	13.6 $\pm$ 1.5	4.48	10.62	1.90	0.236	0.393	+137.82	+164.79
		4.54	8.57	1.76	0.299	0.306	+141.71	+141.71
CD-33 3337	11.6 $\pm$ 0.8	6.73	8.85	2.30	0.061	0.136	+176.20	+184.23
		6.97	8.71	2.25	0.105	0.108	+181.26	+181.26
CD-43 6810	5.3 $\pm$ 1.0	1.96	12.43	5.69	0.375	0.677	+70.25	+112.54
		1.93	9.50	1.76	0.641	0.660	+79.33	+79.33
CD-45 3283	...	1.00	24.99	9.86	0.869	0.921	+22.19	+46.83
		0.99	23.80	10.32	0.866	0.920	+39.13	+39.13
CD-51 4628	6.9 $\pm$ 1.4	2.63	23.57	11.73	0.671	0.791	+92.74	+118.24
		2.65	20.29	11.06	0.707	0.769	+101.96	+101.96
CD-57 1633	10.5 $\pm$ 1.6	0.09	23.61	0.90	0.961	0.989	-13.12	+28.43
		0.20	20.50	15.06	0.794	0.981	+15.06	+15.06
CD-61 282	14.8 $\pm$ 1.9	0.48	17.25	0.19	0.843	0.945	-59.24	-23.26
		0.38	16.86	10.81	0.716	0.956	-26.76	-26.76
G05-19	13.4 $\pm$ 1.4	0.45	21.31	9.08	0.847	0.954	-20.16	-3.93
		0.25	18.96	15.54	0.808	0.973	-16.25	-16.25
G05-36	10.3 $\pm$ 1.0	0.19	11.57	1.82	0.744	0.967	-49.96	-8.60
		0.66	8.91	4.71	0.567	0.862	-37.30	-37.30
G05-40	12.7 $\pm$ 0.7	0.80	12.50	5.67	0.654	0.861	+18.24	+56.77
		0.56	10.47	6.09	0.615	0.897	+32.01	+32.01
G13-38	...	2.38	12.22	4.01	0.505	0.647	+85.21	+119.55
		2.39	9.67	1.86	0.586	0.601	+94.05	+94.05
G15-23	...	1.14	10.19	0.93	0.650	0.758	+47.59	+96.69
		1.53	8.47	0.91	0.682	0.694	+66.23	+66.23
G16-20	...	1.27	15.39	2.10	0.678	0.779	+55.82	+124.48
		2.07	12.67	1.82	0.705	0.719	+93.49	+93.49
G18-28	...	0.35	8.83	4.11	0.585	0.919	+16.04	+52.51
		0.59	8.59	4.64	0.554	0.871	+34.19	+34.19
G18-39	11.4 $\pm$ 1.0	0.03	12.00	4.77	0.701	0.994	-34.64	+2.37
		0.06	11.34	8.30	0.734	0.989	-4.66	-4.66
G20-15	...	5.58	16.90	9.91	0.441	0.495	+158.55	+165.94
		5.76	16.46	9.68	0.448	0.480	+163.07	+163.07
G21-22	12.5 $\pm$ 1.2	0.06	14.31	8.48	0.702	0.991	-12.23	+8.35
		0.05	13.59	10.01	0.732	0.992	-1.37	-1.37
G24-13	11.3 $\pm$ 2.0	5.25	15.10	4.38	0.374	0.474	+173.18	+190.55
		5.30	14.23	4.18	0.443	0.456	+183.30	+183.30
G24-25	...	0.19	12.25	8.24	0.586	0.963	-19.19	+18.45
		0.14	11.54	7.25	0.699	0.976	+8.93	+8.93
G31-55	17.2 $\pm$ 2.1	0.93	12.91	1.89	0.644	0.801	+40.45	+107.95
		1.28	8.57	1.17	0.704	0.740	+59.47	+59.47
G46-31	10.2 $\pm$ 1.1	0.30	11.84	1.25	0.588	0.951	-70.73	-15.94
		1.03	8.63	1.01	0.773	0.786	-48.39	-48.39
G49-19	9.2 $\pm$ 1.3	0.02	8.68	5.37	0.529	0.994	-14.66	+16.24
		0.28	8.72	5.88	0.604	0.936	+15.61	+15.61
G53-41	12.4 $\pm$ 1.2	1.22	9.20	7.19	0.454	0.757	-51.30	-32.37
		1.43	8.66	6.52	0.485	0.712	-38.21	-38.21
G56-30	11.8 $\pm$ 1.4	0.53	9.15	1.68	0.754	0.891	-42.70	-18.39
		0.40	8.73	5.50	0.581	0.913	-24.82	-24.82
G56-36	8.7 $\pm$ 1.4	0.18	12.58	1.43	0.855	0.963	-0.57	+45.59
		0.09	9.27	6.20	0.661	0.981	+6.20	+6.20
G57-07	9.9 $\pm$ 1.4	1.45	9.37	1.11	0.607	0.723	+60.41	+98.45
		1.83	8.95	1.04	0.637	0.660	+78.54	+78.54
G63-26	...	1.01	10.68	1.23	0.618	0.826	-80.45	-45.17
		1.47	9.07	1.03	0.702	0.721	-65.94	-65.94
G66-22	...	0.85	22.52	0.26	0.843	0.900	+46.19	+98.79
		0.91	15.33	0.25	0.887	0.887	+53.54	+53.54

**Table 4.** continued

Star	Age $\pm\sigma$ Age (Gyr)	r <sub>min</sub> (kpc)	r <sub>max</sub> (kpc)	z  <sub>max</sub> (kpc)	e <sub>min</sub>	e <sub>max</sub>	h <sub>min</sub> (/10 km s <sup>-1</sup> kpc)	h <sub>max</sub> (/10 km s <sup>-1</sup> kpc)
G74-32	7.0 $\pm$ 2.3	1.77	13.75	2.85	0.641	0.708	+68.86	+115.26
		2.03	10.50	1.50	0.660	0.675	+87.58	+87.58
G75-31	10.7 $\pm$ 0.5	1.17	16.43	6.39	0.797	0.857	+26.71	+50.89
		0.99	16.06	7.71	0.776	0.884	+40.86	+40.86
G81-02	10.3 $\pm$ 0.6	0.88	11.65	1.43	0.794	0.851	+37.32	+62.39
		0.78	11.09	5.46	0.641	0.869	+44.44	+44.44
G82-05	...	1.05	39.64	2.39	0.906	0.925	+52.28	+109.59
		1.07	25.84	2.65	0.910	0.921	+64.46	+64.46
G85-13	6.8 $\pm$ 2.7	4.44	13.97	0.61	0.469	0.516	+171.43	+182.88
		4.58	14.05	0.60	0.507	0.508	+180.97	+180.97
G87-13	9.7 $\pm$ 0.5	0.42	13.05	1.02	0.891	0.935	-40.03	-17.62
		0.42	12.07	0.20	0.932	0.933	-27.76	-27.76
G94-49	...	2.65	13.41	0.17	0.518	0.611	+103.05	+148.12
		3.30	11.84	0.06	0.564	0.564	+136.01	+136.01
G96-20	...	4.05	12.04	3.89	0.393	0.482	+138.05	+148.69
		4.24	11.13	3.50	0.424	0.448	+140.08	+140.08
G98-53	11.5 $\pm$ 1.1	0.50	11.02	5.12	0.656	0.909	-32.68	-1.82
		0.11	11.27	7.62	0.685	0.981	-7.69	-7.69
G99-21	10.6 $\pm$ 3.3	0.96	9.09	3.75	0.516	0.803	+43.17	+79.31
		1.30	8.89	0.43	0.740	0.746	+61.88	+61.88
G112-43	11.4 $\pm$ 0.5	6.73	20.11	17.42	0.451	0.499	+114.74	+116.87
		6.64	20.16	17.51	0.460	0.503	+115.49	+115.49
G112-44	15.7 $\pm$ 1.5	6.94	20.15	17.20	0.441	0.488	+123.16	+125.21
		6.85	20.20	17.26	0.452	0.492	+123.98	+123.98
G114-42	13.7 $\pm$ 2.8	0.90	33.87	13.99	0.885	0.945	+43.52	+65.40
		0.86	30.63	12.86	0.883	0.945	+47.76	+47.76
G119-64	...	0.98	15.12	5.52	0.783	0.877	-39.24	-25.24
		0.58	14.80	8.33	0.736	0.925	-31.42	-31.42
G121-12	10.5 $\pm$ 1.1	0.94	27.10	10.51	0.864	0.927	+35.80	+54.60
		1.11	25.61	10.42	0.869	0.917	+45.55	+45.55
G125-13	...	0.31	14.39	11.13	0.635	0.946	-3.96	+33.53
		0.36	14.73	9.49	0.703	0.951	+24.00	+24.00
G127-26	10.3 $\pm$ 0.6	3.70	13.63	1.09	0.515	0.570	+148.08	+162.91
		3.79	11.99	0.93	0.518	0.520	+148.83	+148.83
G150-40	11.2 $\pm$ 1.0	0.69	10.74	0.48	0.698	0.880	-66.11	-32.75
		1.10	8.75	0.40	0.774	0.777	-54.35	-54.35
G159-50	12.2 $\pm$ 2.5	1.06	14.20	5.68	0.672	0.842	+45.08	+78.24
		0.99	12.24	5.86	0.681	0.850	+52.97	+52.97
G161-73	10.7 $\pm$ 0.6	0.01	13.68	1.68	0.909	0.999	-22.93	+7.37
		0.03	13.04	9.48	0.701	0.995	-0.02	-0.02
G170-56	10.3 $\pm$ 0.6	0.13	12.94	1.87	0.792	0.979	-40.88	+13.65
		0.49	8.54	4.91	0.569	0.891	-29.53	-29.53
G172-61	...	0.31	8.89	4.19	0.637	0.930	-28.44	-3.52
		0.33	8.60	5.91	0.777	0.926	-11.12	-11.12
G176-53	...	0.01	18.27	2.06	0.933	0.999	-24.29	+24.66
		0.23	13.24	10.19	0.684	0.965	-15.25	-15.25
G180-24	12.3 $\pm$ 1.1	0.00	9.57	0.51	0.942	0.999	-12.29	+11.90
		0.13	9.32	6.95	0.561	0.971	+8.22	+8.22
G187-18	7.9 $\pm$ 2.9	2.58	12.15	2.78	0.484	0.620	+96.88	+127.86
		2.71	9.62	1.30	0.550	0.560	+106.09	+106.09
G188-22	12.9 $\pm$ 1.0	3.25	14.90	1.96	0.575	0.627	+131.26	+159.73
		3.26	12.81	1.55	0.588	0.594	+134.15	+134.15
G192-43	7.4 $\pm$ 1.4	0.32	22.71	0.34	0.947	0.967	+14.29	+36.32
		0.32	20.66	0.42	0.968	0.969	+23.82	+23.82
G232-18	...	0.25	10.09	5.92	0.658	0.944	-3.39	+29.21
		0.15	9.51	6.33	0.639	0.968	+10.66	+10.66
HD3567	11.0 $\pm$ 0.5	0.08	11.66	5.28	0.672	0.985	-19.34	+16.54
		0.08	10.67	7.94	0.663	0.985	-3.71	-3.71

**Table 4.** continued

Star	Age $\pm\sigma$ Age (Gyr)	r <sub>min</sub> (kpc)	r <sub>max</sub> (kpc)	z  <sub>max</sub> (kpc)	e <sub>min</sub>	e <sub>max</sub>	h <sub>min</sub> (/10 km s <sup>-1</sup> kpc)	h <sub>max</sub> (/10 km s <sup>-1</sup> kpc)
HD17820	11.2 $\pm$ 0.9	4.39	10.21	1.87	0.299	0.388	+143.13	+158.37
		4.40	8.79	1.15	0.327	0.333	+144.64	+144.64
HD22879	12.5 $\pm$ 1.2	4.12	12.04	1.24	0.415	0.473	+152.07	+171.06
		4.24	9.90	0.48	0.399	0.400	+151.77	+151.77
HD25704	9.8 $\pm$ 1.3	4.68	11.74	0.06	0.358	0.420	+171.44	+189.87
		4.83	10.61	0.05	0.375	0.375	+171.12	+171.12
HD51754	8.5 $\pm$ 1.7	0.82	15.39	1.00	0.757	0.852	+39.83	+107.67
		1.77	13.83	0.17	0.772	0.773	+88.23	+88.23
HD59329	...	0.61	11.03	0.69	0.671	0.895	-69.69	-29.29
		0.86	9.51	0.54	0.829	0.833	-46.34	-46.34
HD76932	11.7 $\pm$ 0.6	4.47	10.73	1.70	0.241	0.389	+138.10	+167.22
		4.72	8.77	1.31	0.295	0.300	+150.30	+150.30
HD97320	10.8 $\pm$ 0.8	6.19	10.78	0.55	0.220	0.265	+197.90	+207.49
		6.57	10.47	0.38	0.229	0.229	+205.64	+205.64
HD103723	9.9 $\pm$ 0.7	0.59	13.42	3.91	0.564	0.868	+27.62	+96.71
		1.06	8.94	1.21	0.754	0.789	+52.13	+52.13
HD105004	11.6 $\pm$ 1.8	0.21	10.18	5.75	0.652	0.954	+2.02	+24.19
		0.19	9.10	6.33	0.608	0.958	+13.21	+13.21
HD106516	...	4.83	10.15	0.72	0.230	0.343	+156.44	+176.40
		5.07	9.11	0.69	0.283	0.285	+163.81	+163.81
HD111980	14.6 $\pm$ 1.1	0.86	14.26	5.77	0.608	0.848	+29.72	+79.14
		1.28	13.99	1.54	0.812	0.832	+67.08	+67.08
HD113679	13.1 $\pm$ 0.8	0.03	11.98	0.13	0.921	0.995	-22.55	+12.40
		0.29	9.06	0.10	0.938	0.938	-19.40	-19.40
HD114762A	10.1 $\pm$ 0.8	5.10	10.71	1.05	0.139	0.341	+155.46	+184.33
		5.40	9.41	1.02	0.267	0.271	+171.12	+171.12
HD120559	...	5.70	9.80	0.32	0.079	0.255	+171.20	+189.88
		6.28	8.57	0.33	0.153	0.154	+183.36	+183.36
HD121004	8.2 $\pm$ 2.7	0.28	11.45	6.42	0.665	0.939	-3.15	+40.96
		0.14	9.49	6.50	0.623	0.971	+9.83	+9.83
HD126681	...	6.32	9.29	1.04	0.085	0.176	+179.07	+194.96
		7.01	8.57	0.94	0.098	0.100	+191.24	+191.24
HD132475	...	1.92	9.74	1.13	0.561	0.671	-100.58	-81.39
		2.56	8.60	0.86	0.535	0.541	-98.37	-98.37
HD148816	11.7 $\pm$ 0.6	0.14	9.51	8.26	0.425	0.965	-17.42	+18.60
		0.08	9.29	7.33	0.570	0.982	-5.14	-5.14
HD159482	9.8 $\pm$ 1.9	4.61	13.48	2.60	0.420	0.490	+165.71	+177.35
		4.80	13.22	2.47	0.461	0.467	+174.57	+174.57
HD160693	9.2 $\pm$ 1.5	2.88	17.33	3.22	0.626	0.686	+120.00	+147.54
		3.03	14.17	2.64	0.637	0.647	+126.93	+126.93
HD163810	...	0.57	14.42	1.91	0.854	0.916	+29.97	+60.56
		0.90	14.42	1.66	0.860	0.883	+51.93	+51.93
HD175179	8.7 $\pm$ 2.2	3.34	11.72	0.41	0.444	0.528	+123.65	+153.54
		3.41	9.37	0.20	0.466	0.466	+128.45	+128.45
HD177095	15.6 $\pm$ 3.6	1.14	13.33	0.39	0.624	0.758	+48.93	+125.28
		2.29	10.17	0.28	0.632	0.632	+98.58	+98.58
HD179626	14.0 $\pm$ 0.8	0.42	9.07	4.00	0.584	0.912	+5.97	+47.52
		0.59	9.06	4.92	0.569	0.878	+33.75	+33.75
HD189558	13.8 $\pm$ 1.7	3.34	11.70	0.89	0.441	0.523	+121.83	+151.56
		3.32	9.09	0.66	0.463	0.465	+123.01	+123.01
HD193901	14.7 $\pm$ 2.6	0.48	11.74	5.31	0.683	0.911	+5.78	+42.46
		0.25	10.35	6.55	0.687	0.952	+17.50	+17.50
HD194598	8.6 $\pm$ 1.8	0.05	12.94	2.04	0.883	0.990	-20.72	+36.10
		0.18	8.61	5.79	0.621	0.959	-11.66	-11.66
HD199289	12.2 $\pm$ 1.5	4.86	10.61	0.21	0.201	0.350	+157.14	+182.72
		5.39	8.64	0.19	0.231	0.231	+168.46	+168.46
HD205650	15.3 $\pm$ 2.1	3.91	12.00	0.32	0.321	0.463	+133.80	+173.13
		4.28	10.15	0.21	0.407	0.407	+154.85	+154.85

**Table 4.** continued

Star	Age $\pm\sigma$ Age (Gyr)	r <sub>min</sub> (kpc)	r <sub>max</sub> (kpc)	z  <sub>max</sub> (kpc)	e <sub>min</sub>	e <sub>max</sub>	h <sub>min</sub> (/10 km s <sup>-1</sup> kpc)	h <sub>max</sub> (/10 km s <sup>-1</sup> kpc)
HD219617	...	1.29	20.52	0.75	0.787	0.833	+63.21	+123.39
		1.32	13.21	0.63	0.816	0.819	+68.64	+68.64
HD222766	20.9 $\pm$ 1.9	0.98	13.31	0.33	0.752	0.831	+46.78	+89.99
		1.35	11.15	0.09	0.783	0.784	+67.92	+67.92
HD230409	...	2.22	13.50	0.06	0.564	0.636	+90.28	+141.32
		2.84	11.10	0.04	0.592	0.592	+119.38	+119.38
HD233511	...	0.27	11.69	0.67	0.895	0.948	+5.66	+33.55
		0.14	9.76	6.78	0.652	0.970	+9.19	+9.19
HD237822	8.0 $\pm$ 2.2	3.20	10.50	4.71	0.376	0.487	+97.75	+114.41
		3.24	9.35	3.92	0.430	0.485	+105.76	+105.76
HD241253	11.3 $\pm$ 1.6	5.08	9.34	1.86	0.233	0.292	+151.95	+160.14
		5.10	8.69	1.74	0.253	0.259	+154.14	+154.14
HD250792A	...	0.58	16.31	7.04	0.775	0.929	+9.80	+34.85
		0.26	14.61	12.22	0.708	0.964	+14.06	+14.06
HD284248	...	1.53	33.04	3.08	0.876	0.900	+76.56	+117.04
		1.59	26.20	2.81	0.878	0.886	+88.96	+88.96